Highly active Pt₃Rh/C nanoparticles towards ethanol electrooxidation. Influence of the catalyst structure

Caio V.S. Almeida[a,b], Dênis S. Ferreira[c], Haoliang Huang[d], Ana C. Gaiotti[c], Giuseppe A. Camara[c], Andrea E. Russell[d], Katlin I.B. Eguiluz[a,b], Giancarlo R. Salazar-Banda[a,b,*]

[a] Laboratory of Electrochemistry and Nanotechnology, Institute of Technology and Research, 49.032-490, Aracaju, Sergipe, Brazil
[b] Process Engineering Postgraduate Program, Tiradentes University, 49.032-490, Aracaju, Sergipe, Brazil
[c] Instituto de Química, Universidade Federal de Mato Grosso do Sul, CEP 549, 79070-900, Campo Grande, MS, Brazil
[d] School of Chemistry, University of Southampton, University Road, Southampton SO17 1BJ, United Kingdom

ABSTRACT

The electrochemical oxidation of ethanol results in the formation of strongly adsorbed intermediates. Pt–Rh catalysts are proposed as alternatives since they easy the C−C bond breaking. However, the effect of the Pt–Rh structure on the catalytic activity and selectivity to CO_2 is not well understood. Here, we synthesised Pt/C and two different Pt–Rh/C catalyst architectures, an alloy (Pt₃Rh/C) and a bimetallic mixture (Pt₃–Rh/C) to study the effect of catalyst structure on its catalytic activity and on the products formed during the ethanol oxidation in acid media. The nanoparticles were prepared by a modified polyol reduction method using ethylene glycol as a co-reducing agent and Pb as a material of sacrifice, to obtain very small and well-dispersed nanoparticles on the carbon support. Fourier transform infrared spectroscopy and derivative voltammetry was used to give insights about the ethanol oxidation mechanism occurring at the developed catalysts. The samples characterised by X-ray diffraction analysis showed distortions in the Pt lattice parameters for the Pt-Rh alloy structure due to the presence of Rh in the catalyst's composition. Transmission electron microscopy analyses indicate that nanoparticles were well-dispersed on a carbon support, with spherical shapes and small particle sizes (2–3 nm). in situ X-ray absorption spectroscopy data evidence that Pt–Rh interactions produce changes in the Pt 5d band vacancy. The electronic effect is maximized when Pt forms an alloy with Rh, resulting in the highest d-band vacancy of the Pt₃Rh/C. The Pt₃Rh/C catalyst showed the highest activity towards ethanol oxidation, presenting current densities in a quasi-steady-state condition (measured at 600 mV) around 5.2 times higher than the commercial Pt/C (Alfa Aesar). Moreover, the onset potential for ethanol oxidation shifts to more negative potentials (110 mV lower taken at 1 mA cm⁻²) was also observed. In situ FTIR data revealed that Pt/C catalyst favours the formation of acetic acid. The synergistic effect between Rh and the alloy structure results in an easier C−C bond breaking for Pt₃Rh/C, in comparison to Pt₃–Rh mixture, thus favouring CO_2 formation at lower potentials.

1. Introduction

Ethanol is a renewable energy source that can be obtained from the fermentation of raw materials derived from cellulose, such as sugar cane, maize, wheat, and beets, among other [1,2]. Compared with other fuels, ethanol is (i) less toxic, (ii) less permeable through polymeric membranes, (iii) cheap and (iv) easier to store and transport. Together, these characteristics make ethanol a sustainable and attractive alternative for use in low-temperature fuel cells [1,3]. Moreover, its complete oxidation generates 12 electrons per molecule, resulting in greater theoretical energy density (8.6 kW h kg⁻¹) compared to other fuels such as methanol (6.1 kW h kg⁻¹) [4,5].

Platinum is the most studied material for ethanol oxidation because of its ability to adsorb organic molecules. However, the performance of pure platinum is not very satisfactory [6]. In addition, the C−C bond breaking via the electrochemical reaction is not easily attained thus ethanol partial oxidation generates intermediates such as acetaldehyde and acetic acid, which decreases the cell efficiency [7]. The other intermediate that is produced during ethanol electrochemical oxidation is carbon monoxide (CO), which adsorbs onto the electrode surface, poisons the active sites and decreases the electrode catalytic activity [5,8]. Thus, the main challenge for ethanol electrooxidation is to achieve its total oxidation to CO_2 at a low potential.

It is known that alloying Pt with elements such as Ru [9], Sn [3], Rh

---

[2] and Pb [10] increases the catalytic activity concerning liquid fuels oxidation. The synergistic effect of Pt modification with a second element is attributed to the so-called bifunctional mechanism and electronic effects [11–13]. Previous reports show that Pt–Rh alloys can improve CO_2 production (in comparison with Pt) during ethanol electrooxidation [14–16].

Bergamaski et al. [15] reported the influence of Pt–Rh/C catalysts composition for CO_2 production showing an increase in total ethanol oxidation compared to pure Pt/C, driving the reaction for CO_2 formation. Furthermore, the Faradaic current efficiency for ethanol oxidation to CO_2, increased from 8% using pure Pt/C to 50% using $Pt_{47}Rh_{53}$/C catalyst at 700 mV *vs.* RHE (*reversible hydrogen electrode*). With these results, they concluded that electronic effects play a key role in ethanol oxidation mechanism for Pt–Rh/C electrodes [15].

In summary, the product distribution and the dominant reaction pathway of ethanol electrooxidation are very complex and depend on many factors including catalyst material [17,18] and structure [19], applied potential [20], reaction media [21], and others. Thus, additional investigations are required to solve the subjacent structural and electronic principles governing the activities of bimetallic nanoparticles [22].

Alayoglu and Eichhorn [23] reported the synthesis and electrochemical activity of Rh@Pt core–shell, RhPt (1:1) alloy, and Rh + Pt bimetallic nanoparticles. The nanoparticles were prepared using a polyol reduction in ethylene glycol. The three different architectures were evaluated for preferential oxidation of CO in hydrogen using 1.0 wt % Pt loadings in Al_2O_3 supports. It was found that for hydrogen feeds with 0.2% CO and 0.5% O_2 the Rh@Pt catalyst was the most active with complete CO oxidation at 70 °C and very high selectivity at 40 °C with 50% CO conversion. The authors believe the enhancements in activities are directly related to the changes in architectural configurations, which alter the electronic structures of the surface metals and/or facilitate alternate reaction mechanisms relative to pure Pt nanoparticles [23].

Several studies regarding PtRh catalysts for ethanol electrooxidation have been reported [2,14–16,26,27]. However, the information and the understanding of the effect of Pt-Rh structures, such as alloy and bimetallic mixture, on their catalytic activity and the products distribution during the ethanol electrooxidation reaction, are still very scarce. Therefore, to experimentally confirm the importance of catalyst structure, we investigate the catalytic activity and the formation of products during ethanol oxidation in acid media using binary Pt_3Rh/C (alloy) and Pt_3–Rh/C (bimetallic mixture) catalysts.

2. Experimental section

2.1. Chemicals

All chemicals used were analytical grade. Lead chloride (II), $PbCl_2$ (Sigma-Aldrich, 98%), ethylene glycol, $C_2H_4(OH)_2$ (Sigma-Aldrich, 99.8%), ultrapure water (15.6 MΩ/cm, Gehaka, MS2000), Vulcan XC-72R carbon black (Cabot), hexachloroplatinic acid, $H_2PtCl_6\cdot(H_2O)_6$ (Sigma-Aldrich, 99.95%), rhodium chloride, $RhCl_3$. xH_2O (Sigma-Aldrich, 39%), alumina, Al_2O_3 (1 μm, SKILL-TEC), 2-propanol, C_3H_7OH (Sigma-Aldrich, 99.5%), Nitrogen gas (White Martins, 99,998%), Nafion® (Sigma-Aldrich, 5 wt % solution), ethanol, C_2H_5OH (Sigma-Aldrich, 99%), sulfuric acid, H_2SO_4 (Sigma-Aldrich, 99,5%) were used.

2.2. Catalysts preparation

All the catalysts synthesised in this work were obtained with 20% weight of metals for Vulcan XC72R carbon mass, in preparation of 200 mg of catalyst, using ethylene glycol as reducing agent and Pb as a sacrificial reductive specie, considering small modifications in the method established by Li et al., without changes of pH mixture [24]. Pb was used as a sacrificial material, in order to obtain small and well-

dispersed nanoparticles. The choice of Pt:Rh molar ratio was obtained considering the studies of Gupta and Tayal [25], Silva-Júnior et al. [26] and Valério Neto et al. [27].

Initially, Pb nanoparticles were deposited on the carbon support, serving as a sacrificial agent for the deposition of the Pt and PtRh (alloy) nanoparticles. In this synthesis, the proper amount of $PbCl_2$ was dissolved in a mixture of 20 mL ethylene glycol and 10 mL of ultrapure water. After addition of Vulcan XC-72R carbon black, the suspension was stirred for 30 min. The mixture was heated up to 120 °C and kept at this temperature for 24 h to ensure a complete reaction. The resulted slurry was filtered, washed several times with ultra-pure water, and the precipitate was dried in an oven at 80 °C for 4 h. The same separation and drying process was performed for all catalysts.

In sequence, the Pb/C composite was mixed with 0.03861 mol L^{-1} $H_2PtCl_6\cdot(H_2O)_6$ solution to synthesise Pt/C nanoparticles For the preparation of Pt_3Rh/C alloy nanoparticles, the Pb/C composite was mixed with the proper amount of $RhCl_3$. xH_2O dissolved in 0.03861 mol L^{-1} $H_2PtCl_6\cdot(H_2O)_6$ solution. In both cases, the metallic precursors were dissolved and reduced in a mixture of 60 mL of ethylene glycol and 10 mL of ultrapure water. The suspension was stirred for 30 min to obtain a uniform suspension and was heated up to 120 °C and kept at this temperature for 24 h.

For the preparation of the Pt_3–Rh/C (mixture) catalyst, calculated amounts of $PbCl_2$, $RhCl_3$. xH_2O and $H_2PtCl_6\cdot(H_2O)_6$ solution were dispersed with Vulcan XC-72R carbon black in a mixture of 60 mL ethylene glycol and 10 mL of ultrapure water. The suspension was stirred for 30 min to form a uniform slurry and was heated to 120 °C and kept at the constant temperature for 24 h. Finally, a Pt/C catalyst was produced for comparative purposes without the use of Pb as sacrificial species.

In all experiments, Pb was recycled adding concentrated HCl to the solution contained Pb^{2+} ions. The $PbCl_2$ recovered was filtered, washed several times with ultra-pure water, and the precipitate was dried in an oven at 80 °C for 4 h.

2.3. Physical characterisation

The crystalline structure was determined by X-ray diffraction (XRD) analyses performed using a BRUKER diffractometer model D8 ADVANCE, operating with Cu Kα radiation (λ = 0. 15,406 nm). The diffraction patterns were registered every 2θ angles from 20 to 90°, with a scan rate of 3° min^{-1}. The working conditions of the powder diffractometer were 1600 KW, a tension of 40 KV and a current of 40 mA. The crystallographic compositions of the catalysts were determined through the X'Pert HighScore Plus program comparing with reference standards of the Joint Committee on Powder Diffraction Data Standards (JCPDS) database.

The morphology of the catalysts and the particles size of Pt were observed by transmission electron microscopy (TEM) using a FEI Tecnai 12 at an 80 kV accelerating voltage. The composition of the catalysts was determined by SEM-EDS using FEI XL30 ESEM, equipped with UltraDry silicon drift X-ray detector.

X-ray absorption (XAS) measurements were conducted at the B18 beamline of the Diamond Light Source (UK). The samples were finely ground and mixed with boron nitride before being compressed into pellets. XAS spectra of the pellets were recorded in transmission mode at Pt L2-edge, L3-edge and in fluorescence mode at Rh K-edge. Spectra at Pb L3-edge were not recorded because they are largely overlapped with Pt L2-edge. The spectra were collected in H_2(g) atmosphere at room temperature to reduce the surface oxide of the metal, which facilitates the data analysis. Pt or Rh foils were characterised along with the samples in the reference channel for energy calibration. The data reduction and analysis of the XAS spectra were conducted using the Demeter software package (ATHENA and ARTEMIS, respectively) [28]. The edge step of each spectrum was normalized by subtracting the pre-edge with a linear function and the post-edge with a quadratic function. The energy shift was calibrated by choosing the zero crossing of the

second derivative of the reference spectra as E0 and assigning it to the corresponding tabulated value provided by ATHENA.

Extended X-ray absorption fine structure (EXAFS) spectra were obtained by subtracting the corresponding XAS spectra with a background algorithm (AUTOBKG) provided by ATHENA, with $R_{bkg} = 1$. The fitting of EXAFS spectra was performed on ARTEMIS using input parameters of theoretic models from CIF files with or without modification. The amplitude reduction factors were determined to be 0.837 for Pt and 0.829 for Rh from the fitting of the corresponding foil spectra.

2.4. Electrochemical and spectroelectrochemical characterisation

Electrochemical measurements were performed and recorded at room temperature using an Autolab Model PGSTAT 302 N potentiostat/galvanostat controlled by Autolab Nova 2.0 software. Experiments were carried out in a one-compartment glass cell, using a conventional three-electrode set up (half–cell). Glassy carbon electrode (3 mm diameter) was used as a substrate for the electrocatalytic material. A hydrogen electrode in the same solution (HESS) connected by a Luggin capillary was used as the reference and a Pt wire was used as the counter electrode. All potentials are referred to the reversible hydrogen electrode (RHE).

Before each electrochemical measurement, the glassy carbon electrode was polished with Al_2O_3 for cleaning. Afterwards, the electrode was sonicated in an ultrasonic bath (Ultra Cleaner Unique/1450 A) submerged in 2-propanol for 10 min to remove any Al_2O_3 traces.

Nitrogen gas was bubbled in all solutions for 20 min before starting each electrochemical test to create an inert atmosphere and decrease the oxygen partial solubility in the electrolytic solution. The catalyst paste was prepared using 0.003 g of suspension powder catalyst in 1000 μL of ultrapure water and 30 μL Nafion® solution, which was dispersed in an ultrasonic bath. Then, 5 μL of the catalyst suspension was transferred with a syringe injector to a glassy carbon electrode. Finally, the electrode was dried at room temperature.

Cyclic voltammetry experiments were performed between 50 and 800 mV at a scan rate of 500 mV s^{-1} until stationary responses were obtained, then two voltammetric cycles were performed at a scan rate of 10 mV s^{-1} to evaluate the behaviour of each catalyst. Linear sweep voltammetry experiments were performed between 200 and 800 mV at 1 mV s^{-1}. Chronoamperometric experiments were performed at 500 mV for 3600 s. The stability of the catalysts synthesised by a modified polyol reduction method was evaluated by chronoamperometry, applying 600 mV during 100 h. The derivative voltammetry profiles were obtained after the derivation of the first cycle of cyclic voltammetry performed between 50 and 1100 mV at a scan rate of 20 mV s^{-1}. All these experiments were carried out in a 0.5 mol L^{-1} ethanol in 0.5 mol L^{-1} H_2SO_4 solution.

In situ FTIR measurements were carried out by using a Frontier FTIR spectrometer (Perkin-Elmer) equipped with MCT (Mercury-Cadmium-Telluride) detector cooled with liquid nitrogen. Reflectance spectra were collected as the ratio (R/Ro), where R represents a spectrum at a given potential and Ro is the spectrum collected at 50 mV. Spectra were computed from the average of 50 interferograms. The spectral resolution was set to 8 cm^{-1}. The electrochemical infrared cell was fitted with a CaF$_2$ planar window for the collection of bands corresponding to species formed during ethanol oxidation.

A catalyst layer was supported on a gold substrate previously polished to a mirror finish (alumina, 0.05 μm) to obtain good reflectivity. Catalysts were characterised in 0.1 mol L^{-1} HClO$_4$ and transferred to a spectroelectrochemical cell to investigate the electrooxidation of ethanol by *in situ* FTIR. 0.6 mL of ethanol was added to the cell to obtain a concentration of 0.5 mol L^{-1} and spectra were collected during a linear sweep voltammogram ($\nu = 10$ mV s^{-1}). During the experiment, the potential was paused at intervals of 50 mV in the potential range from 50 to 1000 mV *vs.* RHE, during which the spectra were collected.
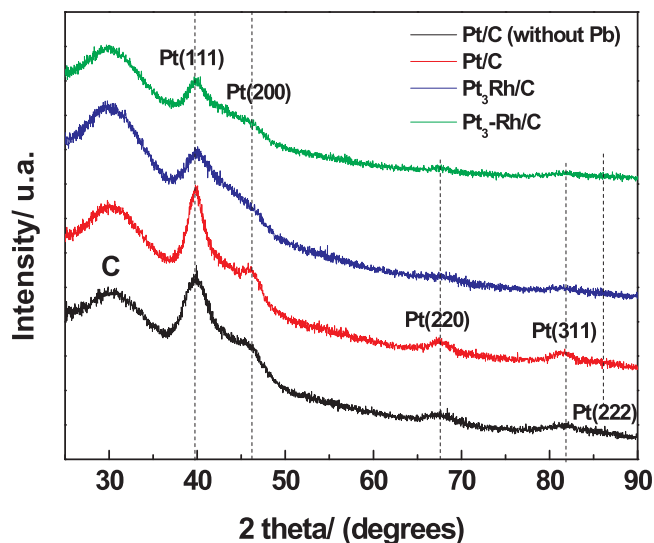

Fig. 1. XRD patterns of Pt/C (without Pb), Pt/C, Pt$_3$–Rh/C and Pt$_3$Rh/C catalyst. Synthesized by modified polyol reduction method and dispersed in Vulcan XC-72R carbon.

In all electrochemical experiments, the current values were normalized by Pt electrochemically active area determined by integration of the charge found in the hydrogen desorption process. A total charge of 210 μC cm^{-2} was assumed for the formation of a hydrogen monolayer adsorbed on Pt surface [29].

3. Results and discussion

3.1. Physical characterisation

XRD patterns of Pt/C (without Pb), Pt/C, Pt$_3$-Rh/C and Pt$_3$Rh/C catalysts are shown in Fig. 1. The first large peak located at the 2θ ̃ 30° is attributed to the (002) plane of the hexagonal structure of carbon support (JCPDS N°00-001-0640). The other five diffraction peaks found in all the catalysts were ascribed to diffractions peaks of Pt (111), Pt (200), Pt (220), Pt (311) and Pt (222) planes (JCPDS N°00-001-1190), respectively, which represent the characteristics of face centred cubic structure of platinum [23]. For Pt/C the Pt planes are observed at 2θ values of 39.9°, 46.5°, 67.6°, 81.6° and 86.2°. Diffraction peaks in all spectra of Fig. 1 are poorly defined, suggesting that the catalysts have very small particle size [28,30].

No reflection peaks for Pb or the Pt-Pb alloy appear in Fig. 1 for the binary catalysts, suggesting the total dissolution of Pb during the syntheses. The peaks angles of Fig. 1 for Pt/C are similar to pure Pt/C (without Pb). For Pt$_3$–Rh/C no peaks corresponding to Rh were observed because of the possible overlap with the Pt peaks [13]. However, no displacement of the peaks referred to the polycrystalline Pt was observed for Pt$_3$–Rh/C. This can be due to the existence of a bimetallic mixture of Pt and Rh.

For Pt$_3$Rh/C the peaks are observed at more positive values of 2θ at 40.2°, 46.8°, 67.9°, 81.9° and 87.1°. Such displacements can be attributed to the existence of a PtRh alloy, with a contraction of the crystalline lattice of Pt [31] due to the substitution of some atoms of Pt by Rh atoms that have smaller sizes ($r_{Rh} = 0.134$ nm against $r_{Pt} = 0.139$ nm) [32].

In addition, Pt and Rh have very close diffraction peak positions due to their similar crystalline structure. Both metals have face-centred cubic structure, belonging to space group Fm3m, and possess similar lattice constants (0.3923 and 0.3803 nm, for Pt and Rh, respectively). The similarity in lattice parameters, and the peak broadening due to small particle size, makes it difficult to distinguish Pt from Rh peaks [33,34].
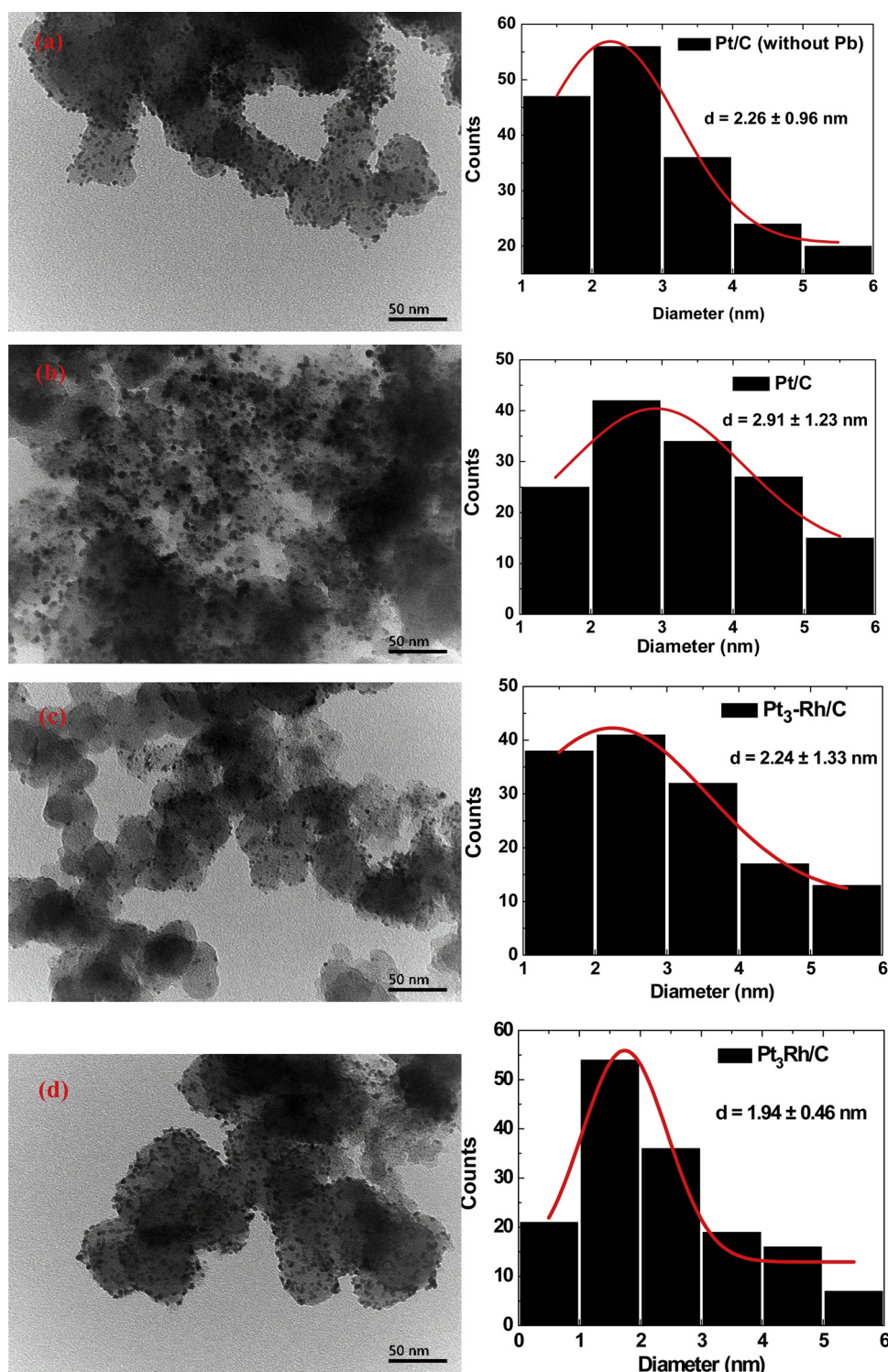
Fig. 2. (Left) TEM images and (Right) the corresponding particle size distribution histograms of (a) Pt/C (without Pb), (b) Pt/C, (c) Pt_3–Rh/C and (d) Pt_3Rh/C catalysts.

Fig. 2 shows TEM images (left) and their corresponding particle size distribution histograms (right) for Pt/C (without Pb), Pt/C, Pt_3–Rh/C and Pt_3Rh/C catalysts. TEM images neither show remarkable differences in shape nor in particle size for the whole series. The metal nanoparticles have a spherical shape and are apparently homogeneously dispersed on the surface of the carbon support.

The mean particle sizes determined from the TEM images and their corresponding standard deviations were: 2.91 ± 1.23, 2.29 ± 0.94, 2.24 ± 1.33 and 1.94 ± 0.46 nm, respectively for Pt/C, Pt/C (without Pb), Pt_3–Rh/C and Pt_3Rh/C. Note that the particle sizes of the Pt_3Rh/C alloy are smaller and present a narrower dispersion, which can be attributed to the contraction of the crystalline lattice of Pt due to the presence of Rh.

The Pt:Rh molar ratios taken from SEM-EDX measurements (Fig. S1) were 3.47:1 and 2.94:1 for Pt_3Rh/C and Pt_3–Rh/C composites, respectively. Note that these molar ratios are close to the nominal one, demonstrating the feasibility of the synthesis method adopted. Moreover, only pure Pt was observed for the Pt/C composite.
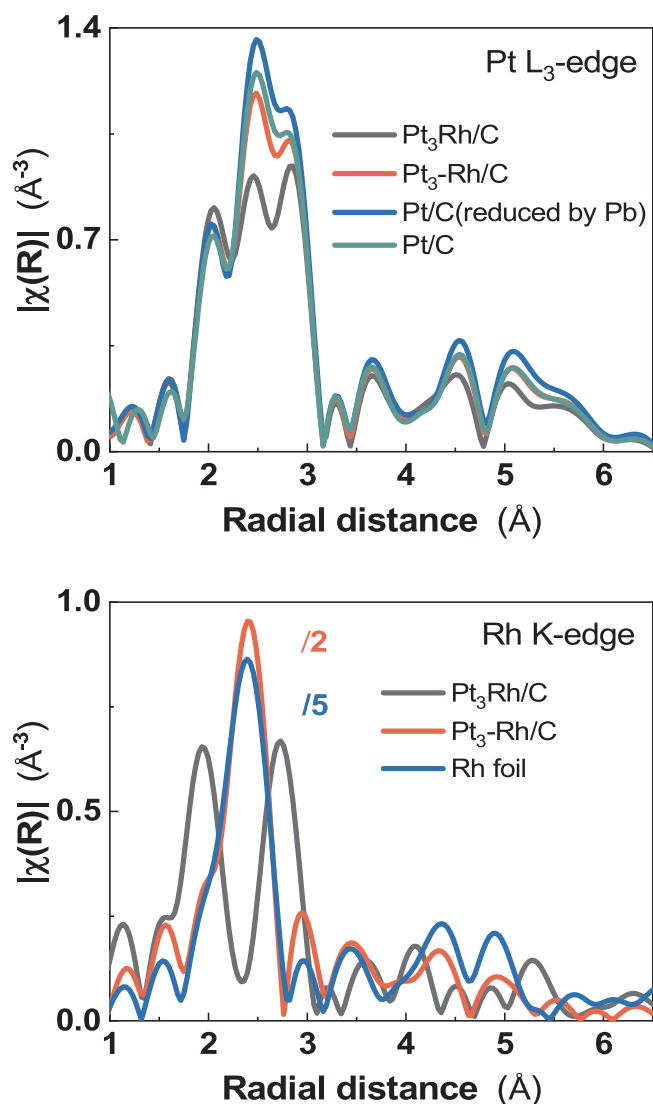
Fig. 3. Fourier transforms of k^2-weighted EXAFS spectra of Pt_3Rh/C and Pt_3–Rh/C at (left) Pt L_3-edge and (right) Rh K-edge, along with Pt/C and Rh foil as the references. The Fourier transformation was performed within a k-range of 3.0–12.6 Å^{-1} for the Pt L_3-edge data, and of 3.3–12.2 Å^{-1} for the Rh K-edge ones. The magnitudes of Rh foil and Pt_3–Rh/C data in Rh K-edge were adjusted for clarity. The spectra are not phase-corrected.

Table 1
Structural parameters of Pt_3-Rh/C, Pt_3Rh/C, Pt/C (reduced by Pb) and Pt/C.

Sample	Scattering path[a]	N[b]	R (Å)[b]	σ^2 x 10^3 (Å^2)[b]	R factor (%)
Pt_3-Rh/C	Pt–Pt	9.9(5)	2.756(2)	5.8(3)	0.9
	Rh–Rh	6.3(7)	2.693(4)	4.7(7)	1.6
Pt_3Rh/C	Pt–Pt	9.2(4)	2.747(4)	5.6(3)	2.2
	Pt–Rh	0.7(3)	2.71(1)[c]	3(2)[c]	
	Rh–Rh	1(4)	2.68(5)	0.7(146)	
	Rh–Pt	5(4)	2.71(1)[c]	3(2)[c]	
Pt/C (reduced by Pb)	Pt–Pt	9.9(5)	2.759(2)	5.2(3)	0.8
Pt/C	Pt–Pt	9.9(5)	2.758(2)	5.6(3)	0.7
Pt foil	Pt–Pt	12[d]	2.7651(4)	4.8(1)	1.6
Rh foil	Rh–Rh	12[d]	2.688(2)	3.7(3)	1.4

[a] The Pt-Pt and Rh-Rh scattering paths were calculated using the crystal structure of Pt (ICSD 52250) and Rh (ICSD 52252), respectively. The heteroatomic scattering paths, Pt-Rh and Rh-Pt, were obtained from modified Pt crystal or Rh crystal input files, in which all the scattered atoms were replaced by the one different from the absorber, with the unit cells of these two models set as the same lattice parameter of 3.875 Å, the average between Pt and Rh. Only the first single scattering paths of each edge are present.

[b] N, the coordination number for the absorber-backscatterer pair; R, the average scattering distance; σ^2, the mean square relative displacement.

[c] The bond length R and its mean square displacement of Rh-Pt are set as the same as those of Pt-Rh, respectively.

[d] Not allowed to vary.

sacrificial element, which was not retained in the final catalyst particles.

For the EXAFS spectrum of Pt3-Rh/C catalyst, the similarities with those of pure metals were found in both Pt L3-edge and Rh K-edge (Fig. 3). The fits of Pt_3–Rh/C (Fig. S3 top, Table 1), using the multiple-shell model, show that no contributions from Pt-Rh and Pt-Pb scattering paths were required at the Pt edge nor Rh-Pt or Rh-Pb at the Rh edge. These confirm that the Pt and Rh of Pt_3–Rh/C are in form of separate Pt and Rh nanoparticles, A small difference between the data and fit is observed at low k component for the Rh K-edge spectrum, which probably a contribution from oxygen neighbours arising from the presence of some surface oxide. This Rh-O was not included in the final fit presented as the effect on the final fit was insignificant.

Whilst the Pt–Pt first coordination number for the Pt_3–Rh/C catalyst is 9.9, which is equal to that of Pt/C and in an agreement of the particle sizes observed by TEM, which of Rh–Rh is only about 6.3. This very small value arises from self-absorption in the XAS spectrum collected at the Rh K-edge for this sample. Thus, whilst the presence or absence of scattering paths can be used to indicate whether the coordination is presently supporting the conclusion that the Pt and Rh are present as separate nanoparticles in this sample and the distances remain reliable, no further interpretation of the coordination numbers at the Rh edge will be presented below.

Significant differences in the local coordination environments are shown in the Pt_3Rh/C catalyst (Fig. 3), with a short scattering path contributed in Pt L3-edge data and a split peak in Rh K-edge data. The fits for the EXAFS data at both edges included the bimetallic paths (Fig. S3 bottom, Table 1). The Pt-Rh path calculated in the fit for the Pt-edge data was used to constrain the corresponding Rh–Pt scattering path in terms of half scattering distance and mean square relative replacement, thus, $R_{Pt–Rh} = R_{Rh–Pt}$ and $\sigma^2_{Pt–Rh} = \sigma^2_{Rh–Pt}$. As in the case of the Pt/C and Pt_3-Rh/C catalysts, no contributions from Pt-Pb or Rh-Pb were observed. The first shell Pt–Pt coordination number of 9.2, is slightly smaller than that for the other samples, in agreement with the particle size trend for observed in the TEM images. The coordination numbers of Pt–Rh, Rh–Pt and Rh–Rh scattering are 0.7, 5 and 1, respectively. The EXAFS fits thus suggest that the structure of Pt_3Rh/C is thus mostly a Pt–Rh alloy with some Rh aggregation.

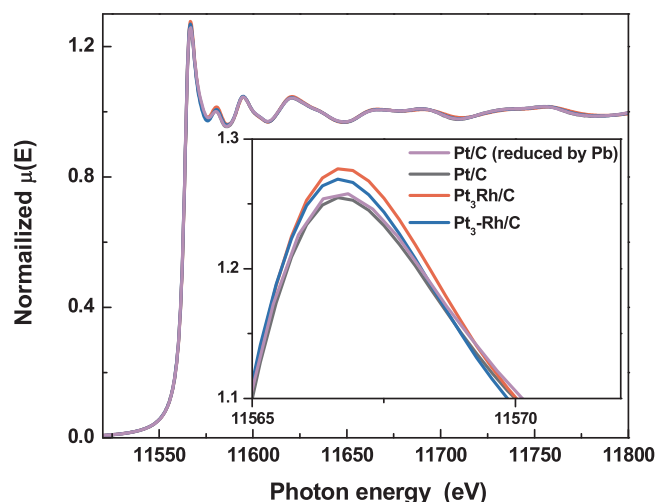The EXAFS data provide some further insights into the preparation

The EXAFS spectra at the Pt L$_3$-edge and Rh K-edge provide structural information about the average local coordination environment of each atom in the samples. Fig. 3 compares the Fourier transforms of the EXAFS of the as-prepared samples with those of the reference samples. The fits, plotted in χ(k) spectra and the corresponding Fourier transforms in magnitude and the real part, are shown in Figs. S2 and S3. The fitting for the Pt L$_3$-edge data and the Rh K-edge data, except for the Pt3Rh/C, are based on a multiple-shell model reported by Inwood recently [35] using the Pt metal (ICSD No. 52250) and Rh metal (ICSD No. 52252) input files to create the scattering paths, which is applicable to pure metal nanoparticles adopting a face-centred-cubic structure (see Table S1 for the constraints used in this model). A single shell model was used to fit the Pt$_3$Rh/C data (Fig. S3 bottom).

The EXAFS for the Pt/C catalyst (Figs. 3 and S2, Table 1) shares the same shape with that of the one synthesized without Pb, and was fitted very well using only Pt neighbours, yielding a Pt-Pt first shell coordination number of 9.9. No additional contributions related to Pt-Pb scattering were required and, thus EXAFS data (Table S2) support the observation from the SEM-EDX (Fig. S1) that the Pb was indeed a

Fig. 4. XANES spectra and (inset) the enlargement around the whiteline region of Pt/C (without Pb), Pt/C, Pt$_3$–Rh/C and Pt$_3$Rh/C catalysts.

Fig. 5. Cyclic voltammogram curves (second cycle) of Pt/C Alfa Aesar, Pt/C, Pt$_3$–Rh/C and Pt$_3$Rh/C catalysts. Measurements were carried out in 0.5 mol L^{-1} H$_2$SO$_4$ at room temperature and a scan rate of 10 mV s^{-1}. ($\rightarrow$) Anodic sweep and ($\longleftarrow$) Cathodic sweep.

of the catalysts. For the Pt$_3$-Rh/C sample, the two metal precursors were expected to be reduced at once; however, they were formed as separated Pt and Rh nanoparticles. The reducing electrode potential of [PtCl$_6$]$^{2-}$ to [PtCl$_4$]$^{2-}$ is 0.68 V, and that of [PtCl$_4$]$^{2-}$ to Pt is 0.755 V. They are higher than that of [RhCl$_6$]$^{3-}$ to Rh (0.431 V), and that of PbCl$_2$ to Pb (–0.2675 V). Moreover, the reducing ability of ethylene glycol is relatively weak, especially in low pH. These two factors possibly lead to the stepwise reduction of the metal precursor and then the separation among metals.

The reduction of Pt and Rh is different in Pt$_3$Rh/C. Pb/C was used to reduce these two metal precursors and the metallic Pb is a strong reducing agent. This allowed Pt and Rh simultaneously deposit on Pb *via* galvanostatic replacement, according to Eq. 1.

$$[PtCl_6]^{2-} + [RhCl_6]^{3-} + Pb \rightarrow PtRh + PbCl_2 \qquad (1)$$
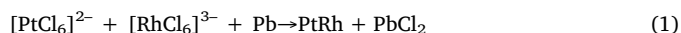
The XANES spectra at Pt L3-edge (Fig. 4) reflect the relative d-band vacancies of the catalyst nanoparticles. The whiteline intensity varies in the order of Pt$_3$Rh/C > Pt$_3$–Rh/C > Pt/C ≈ Pt/C (without Pb). The whiteline of Pt L3-edge describes the electron transition from 2p$_{3/2}$ to the available 5d$_{5/2}$, and thus the intensity of whiteline is proportional to the 5d vacancy of Pt.

As the EXAFS spectra suggest, the as-prepared samples are Pt nanoparticles for Pt/C, Pt and Rh nanoparticles for Pt$_3$–Rh/C, and Pt–Rh alloy nanoparticles for Pt$_3$Rh/C. The XANES spectrum of Pt/C is well-matched with that of Pt/C (without Pb), in good agreement with the actual structure of Pt/C. In the case of Pt and Rh nanoparticles, based on the synthesis, they are probably close with each other, which allows some electron transfer between them. Thus, the 5*d* electrons of Pt may partly transfer to Rh, which has fewer *d* electrons and is more electronegative. This electronic contact is maximized when Pt form an alloy with Rh (Pt$_3$Rh/C), resulting in a greater *d*-band vacancy.

3.2. Electrochemical characterisation

Fig. 5 shows cyclic voltammograms for all catalysts in the absence of ethanol. It was possible to identify two well-defined regions within the potential range of 50 mV and 800 mV *vs.* RHE, typically of polycrystalline Pt, as evidenced by the XRD patterns (Fig. 1).

In the first region between the potentials of 50 and 400 mV (*vs.* RHE) hydrogen adsorption (cathodic sweep) and oxidation of adsorbed hydrogen adsorbed (anodic sweep), are seen. The hydrogen adsorption and desorption equations are described as:
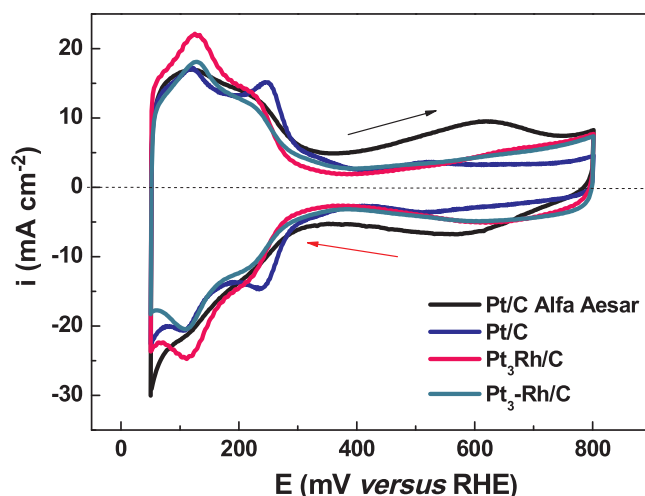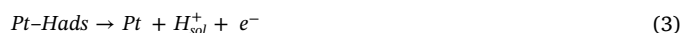
$$Pt + H_{sol}^+ + e^- \rightarrow Pt–Hads \qquad (2)$$

$$Pt–Hads \rightarrow Pt + H_{sol}^+ + e^- \qquad (3)$$

In the second region between 400 and 800 mV, the electrode behaviour resembles that of an ideally polarized one, due to ions storage in the electric double layer, presenting mostly capacitive currents, that is, no surface reaction happens in this potential range [36–39].

In addition, in Fig. 5, the hydrogen desorption for Pt/C and bimetallic catalysts showed well-defined peaks. The strong sensitivity and activity of hydrogen desorption lead to speculate that synergistic effects between the metals nanoparticles increases surface sensitivity and activity [40], which accelerates the kinetics of hydrogen desorption [41].

The higher definition of the adsorption/desorption peaks for Pt/C compared to the Pt/C Alfa Aesar catalyst may be attributed to changes in the Pt crystal lattice due to the reduction caused by Pb atoms. It is considered that well-defined peaks in this region are derived from desorption of hydrogen atoms from Pt sites with well-defined crystalline lattice [42].

Pt$_3$–Rh/C and Pt$_3$Rh/C catalysts showed changes in hydrogen desorption/adsorption region when compared to Pt where a more intense peak at 150 mV is observed for these catalysts. According to Lima et al., [43] in case of Rh-containing catalysts, the adsorption/desorption region is characterised by a single intense peak, which may be associated with hydrogen adsorption/desorption in an intermetallic Pt–Rh phase. The less intense peak located at 200 mV can be associated to a Pt–H phase [28,44].

A good catalyst for ethanol oxidation should be the one that produces the highest current values at the lowest potentials. Another important issue is that the catalyst must be resistant to poisoning and CO accumulation on its surface and/or allow its accumulation to be as low as possible [45].

Fig. 6a shows cyclic voltammograms for all catalysts in the presence of ethanol. For all catalysts, the hydrogen adsorption region is inhibited (between 50 mV and 400 mV *vs.* RHE). The active sites are suppressed by adsorbates from alcohol decomposition formed on Pt surface [3,45], since acetic acid, one of the main coproducts of ethanol oxidation, adsorbs strongly on the electrode surface and hinders the reaction, as proposed by Iwasita [45].

The current density values estimated at 600 mV indicate superior specific activities for Pt$_3$–Rh/C and Pt$_3$Rh/C catalysts in comparison to Pt/C and Pt/C Alfa Aesar catalysts. The specific activity for ethanol oxidation was as follows, in decreasing order: Pt$_3$Rh/C > Pt$_3$–Rh/C Pt/C > Pt/C > Pt/C Alfa Aesar. Higher current densities indicate that higher amounts of ethanol are being oxidised [16,46].
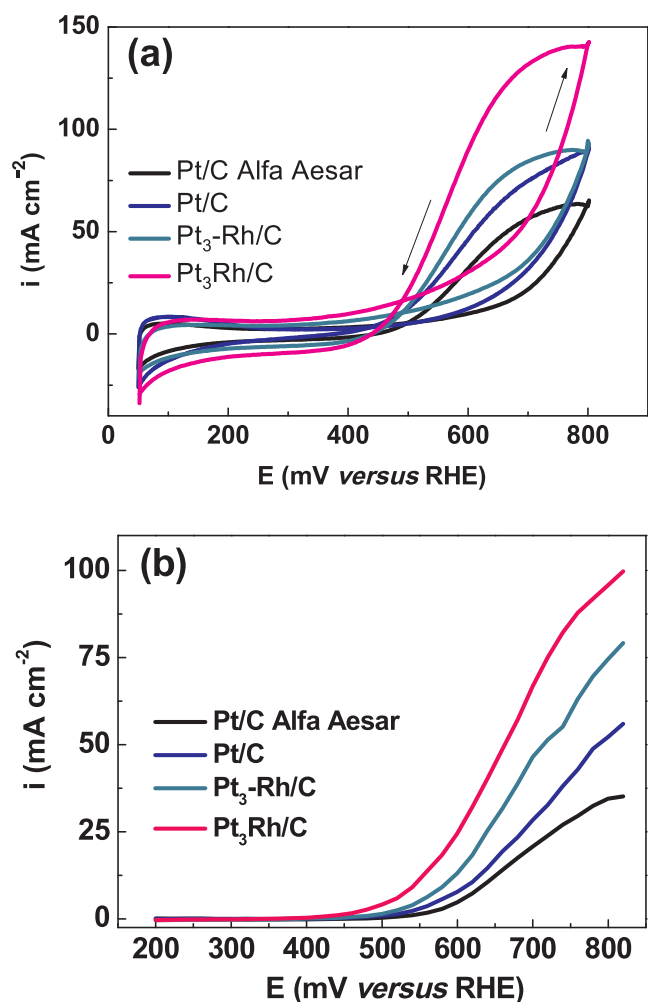
Fig. 6. (a) Cyclic voltammogram curves (second cycle) of Pt/C Alfa Aesar, Pt/C, Pt$_3$–Rh/C and Pt$_3$Rh/C catalysts taken in 0.5 mol L^{-1} H$_2$SO$_4$ and 0.5 mol L^{-1} ethanol at room temperature and a scan rate of 10 mV s^{-1}. (b) Linear sweep voltammograms for ethanol oxidation on Pt/C Alfa Aesar, Pt/C, Pt$_3$–Rh/C and Pt$_3$Rh/C catalysts taken in 0.5 mol L^{-1} H$_2$SO$_4$ and 0.5 mol L^{-1} ethanol at room temperature and a scan rate of 1 mV s^{-1}.

Although a straightforward comparison of data from different studies is difficult because of different experimental conditions, we compare our results with several reports focused on Pt-Sn and Pt-Ru catalysts, benchmark anode catalysts of this field of study. The current density values at 600 mV vs. RHE for PtRh catalysts (30.5 mA cm^{-2} for Pt$_3$Rh/C and 19.3 mA cm^{-2} for Pt$_3$–Rh/C) were much higher than the values reported by Li and co-workers [47] for PtSn and PtRu developed catalysts. During the cyclic voltammograms for the oxidation of ethanol (1.0 mol L^{-1}), the current density values obtained at 600 mV were around 2.5 and 5.0 mA cm^{-2} for PtRu/C and PtSn/C, respectively. The tests were performed at a sweep rate of 25 mV s^{-1} in 0.5 mol L^{-1} HClO$_4$

In another study, Li and Pickup [54] prepared carbon-supported Pt–Sn catalysts with different ratios of Pt to Sn. The catalysts were prepared by decorating an E-Tek 20% Pt on C catalyst with Sn. It was found at 600 mV, current densities between 1.0 and 2.0 mA cm^{-2} by linear sweep voltammetry (LSV) for oxidation of 1.0 mol L^{-1} ethanol in 0.1 mol L^{-1} H$_2$SO$_4$ at 10 mV s^{-1}, respectively for Pt/Sn (8:1) and Pt/Sn (4:1) catalysts. The current density for the best catalyst, Pt/Sn (4:1), is roughly 9.8 and 15.3 times lower than the values reported in our work for Pt$_3$–Rh/C and Pt$_3$Rh/C, respectively. Colmati and co-workers [55] prepared carbon supported Pt–Sn alloy catalysts by formic acid reduction and compared their catalytic activity for the oxidation of ethanol with the commercial Pt/C E-TEK and Pt$_3$Sn/C E-TEK catalysts. The

current density, taken at 600 mV for ethanol oxidation in LSV experiments (10 mV s^{-1}) at room temperature for Pt$_3$Sn/C E-TEK (30 mA cm^{-2}), is similar to our measurements; however, their measurements were done in a higher ethanol concentration (1.0 mol L^{-1}), which increases the ethanol oxidation rate.

Fig. 6b shows the linear sweep voltammograms recorded for all catalysts performed at low scan rate (1 mV s^{-1}) to achieve a quasi-steady-state condition, and consequently, stationary currents in order to appropriate comparison the catalytic activity of catalysts. The trend in catalytic activity for ethanol oxidation is similar to that recorded during the cyclic voltammetry experiments, the bimetallic PtRh catalysts developed better performance than Pt/C and Pt/C Alfa Aesar catalysts towards ethanol oxidation.

The onset potential for ethanol oxidation taken for Pt/C, Pt$_3$–Rh/C and Pt$_3$Rh/C catalysts, measured at 1 mA cm^{-2}, shifted in 20, 60 and 110 mV to more negative potentials compared to the commercial catalyst, respectively. Furthermore, these catalysts display current densities (measured at 600 mV vs. RHE) 1.6, 2.8 and 5.2 times higher than Pt/C Alfa Aesar. The enhanced activity of the Pt$_3$Rh/C catalyst may be attributed to the presence of Rh, which could favour the C−C and C−H bond breaking, facilitating ethanol oxidation and CO$_2$ formation [48,49].

Furthermore, a clear correlation between ethanol oxidation catalytic activity and electronic properties is evidenced by XANES data (Fig. 4). The highest catalytic activity observed for the Pt$_3$Rh/C catalyst can be explained by the larger Pt 5d band electronic vacancy, in other words, by an emptier 5d band. Thus, Rh modifies Pt electron structure changing the Fermi electronic density level in such a way that the Pt-adsorbate interaction is also weakened, thus lowering the energy barrier for the oxidation of adsorbates [32,50].

Another possibility for the higher catalytic activity observed for Pt$_3$Rh/C may be related to particle size. Some studies reported an increase in ethanol oxidation activity with decreasing particle size [51,52]. The effect was ascribed firstly to increase of activity area, since smaller particles can have a higher fraction of surface atoms interacting with the carbon support than larger particles, thus enhancing the charge transfer between carbon support and metallic centres. Secondly, the high ability of small particles to oxidise adsorbed intermediates can be partially ascribed by the high amount of adsorbed OH at lower potentials. As in the case of the oxidation of CO on PtRh, the increase in the oxophilicity with decreasing particle size results in an increase in the ethanol oxidation activity [53]. Then, the adsorbed OH can act as a promoter of ethanol oxidation on Pt/C (d = 2.91 ± 1.23 nm) and Pt$_3$Rh/C (d = 1.94 ± 0.46 nm), according to Fig. 2.

Another point worthy of note is that Pt$_3$–Rh/C is less active than Pt$_3$Rh/C for ethanol oxidation, probably because monometallic Rh surfaces are less efficient than Pt$_3$Rh alloys for the alcohol dehydrogenation reaction. A higher energy barrier for dehydrogenation in monometallic Rh surfaces can difficult the C−C bond scission to form CO, thus leading to a lower oxidation reaction rate, confirming that the enhancements in activities are directly related to the changes in catalyst structure [15,23].

The derivative voltammetry technique shows the rate voltammetric current change, I, with respect to the potential of the electrode, E, dI/dE. The feasibility of this technique to determine the electrocatalytic activity towards ethanol oxidation has been demonstrated in the literature [16,53]. The derivative technique has an improved signal-to-noise ratio, the voltammetric peak location accuracy and alcohol onset potential determination compared with cyclic voltammetry also revealing insights of the mechanism for alcohol oxidation [46].

For Pt/C Alfa Aesar and Pt/C, the derivative voltammograms of Fig. 7 are quite similar, which suggests similar reaction mechanisms, where at low potentials, from point a to point b, dissociative adsorption of ethanol occurs with the subsequent removal of hydrogen atoms from the molecule, as shown in the following equations:
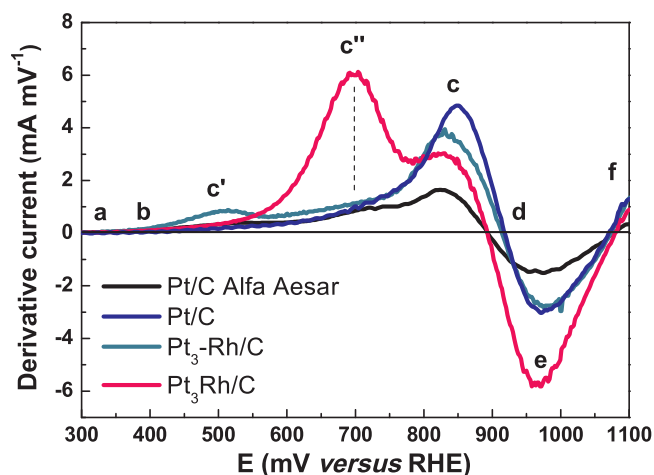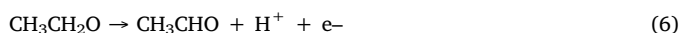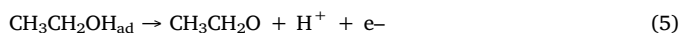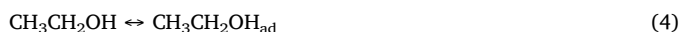
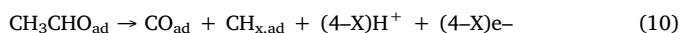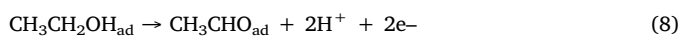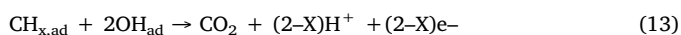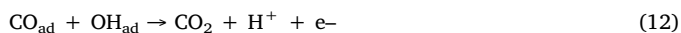**Fig. 7.** Derivative voltammograms of the ethanol oxidation reaction for Pt/C Alfa Aesar, Pt/C, Pt$_3$Rh/C and Pt$_3$–Rh/C in 0.5 mol L^{-1} H$_2$SO$_4$ + 0.5 mol L^{-1} ethanol solution at 20 mV s^{-1}. With letters a, b, c, c', c'', d, e, f showing the various potential regions and mechanistic aspect of ethanol oxidation.

$$CH_3CH_2OH \leftrightarrow CH_3CH_2OH_{ad} \tag{4}$$

$$CH_3CH_2OH_{ad} \rightarrow CH_3CH_2O + H^+ + e- \tag{5}$$

$$CH_3CH_2O \rightarrow CH_3CHO + H^+ + e- \tag{6}$$

$$CH_3CHO \rightarrow CH_3CO + H^+ + e- \tag{7}$$

Several parallel reactions can also occur at this low potential with the production of various adsorbed compounds, like acetyl and acetate groups, without the C−C bond cleavage (Eqs. 8 and 9), or CO and CH$_3$, resulting from C−C bond cleavage (Eqs. 10 and 11) [56]. Most of the Pt active surface is then covered with adsorbed reaction intermediaries. The derivative current gets close to zero at ˜400 mV (point b), and the dissociative oxidation of ethanol can be considered as the rate-determining step at lower potentials. Nevertheless, from Fig. 7, this region is shorter for binary and ternary catalysts, and point b is around 50 mV more negative than for Pt/C and Pt/C Alfa Aesar. Note that the shift to more negative potentials at the binary compositions compared to Pt/C and Pt/C Alfa Aesar was also observed in Fig. 6.

$$CH_3CH_2OH_{ad} \rightarrow CH_3CHO_{ad} + 2H^+ + 2e- \tag{8}$$

$$CH_3CHO_{ad} \rightarrow CH_3CHO \tag{9}$$

$$CH_3CHO_{ad} \rightarrow CO_{ad} + CH_{x,ad} + (4–X)H^+ + (4–X)e- \tag{10}$$

$$CH_3CH_2OH_{ad} \rightarrow CO_{ad} + CH_{x,ad} + (6–X)H^+ + (6–X)e- \tag{11}$$
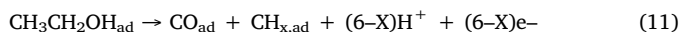
From point b to point c, due to the increase in potential, the adsorbed intermediates, possibly CO and CH$_x$ are oxidized to CO$_2$, as shown in Eqs. 12 and 13. In turn, water hydrolysis (Eq. 14) provides active oxygen species, essential for ethanol oxidation to CO$_2$.

$$CO_{ad} + OH_{ad} \rightarrow CO_2 + H^+ + e- \tag{12}$$

$$CH_{x,ad} + 2OH_{ad} \rightarrow CO_2 + (2–X)H^+ + (2–X)e- \tag{13}$$

$$H_2O \rightarrow OH_{ad} + H^+ + e- \tag{14}$$

Less oxidized compounds, such as acetyl and acetate species react to form acetic acid by two different pathways, according to Eqs. 15 and 16, freeing more sites to continue the reaction. Although the shape of the derivative voltammogram taken for Pt/C Alfa Aesar and Pt/C are very similar, the dI/dE in point c is higher for Pt/C, indicating a larger catalytic surface.

$$CH_3CO_{ad} + OH_{ad} \rightarrow CH_3COOH \tag{15}$$

$$CH_3CHO_{ad} + OH_{ad} \rightarrow CH_3COOH + H^+ + e- \tag{16}$$
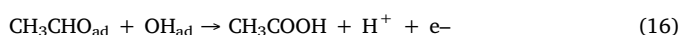
The next process is characterised by a decrease in the dI/dE values from point **c** to point **e**. An increase in potential results in the generation of OH in the Pt sites, which tends to block the adsorption of ethanol and its subsequent oxidation. The oxidative removal of OH$_{ad}$ may be considered as the rate-determining step in this stage. At point d, the dI/dE values reach zero.

The derivative current values become negative after point d, because the effect of OH$_{ad}$ is now detrimental. As OH species are strongly adsorbed to Pt sites, they hinder ethanol adsorption. At point e, dI/dE reaches its lowest value, where the active sites of the catalysts are almost completely covered by OH$_{ad}$.

Thus, the increase in the dI/dE values from point e to point f can result from the reaction of previously adsorbed species on the surface to form acetic acid and/or the oxidation of acetic acid to CO$_2$. In addition, the preferential pathway on Pt (111) is the reaction to form acetate and acetic acid [58–60]. The formation of undesirable acetic acid and their use must be avoided since it reduces the fuel cells efficiency [41].

On the other hand, the derivative voltammograms for Pt$_3$–Rh/C and Pt$_3$Rh/C (Fig. 7) have different shapes when compared to pure Pt catalysts. New designated c' and c" peaks appear, representing a change in the oxidation mechanism or the appearance of new parallel reactions.

For Pt$_3$–Rh/C, peak c' can be ascribed to the formation of reaction intermediates. According to Guillém-Villafuerte et al., for potentials > 400 mV, acetaldehyde production may occur after removing hydrogen atoms from ethanol [57] (Eq. 6). However, the peak of ethanol oxidation for Pt$_3$–Rh/C occurs in the same potential for pure platinum catalyst [18].

The new peak, c", for Pt$_3$Rh/C could be related to the direct ethanol oxidation to CO$_2$ *via* the oxidation of CO and CH$_x$ (Eqs. 11 and 12) [51]. For Pt$_3$Rh/C, c" reaches the highest current density at 700 mV, whilst for the other catalysts, it occurs at 850 mV. Such difference suggests an easier C−C bond break and a higher preference for CO$_2$ production [18], which can be ascribed to the presence of Rh and the alloy structure to facilitate the oxidation of ethanol [26].

At low potentials, Pt is not able to produce OH species. Fast CO$_{ad}$ oxidation in binary catalysts at low potential results in ethanol oxidation, predominantly by a series of mechanisms (Eqs. 17 and 18), where M = Rh [48].
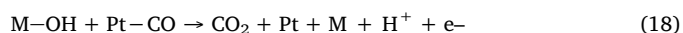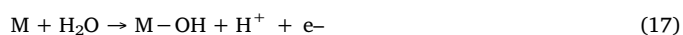
$$M + H_2O \rightarrow M−OH + H^+ + e- \tag{17}$$

$$M−OH + Pt−CO \rightarrow CO_2 + Pt + M + H^+ + e- \tag{18}$$

Fig. 8 shows the chronoamperometric tests for ethanol oxidation carried out at 500 mV *vs.* RHE. For all curves, the faradaic current
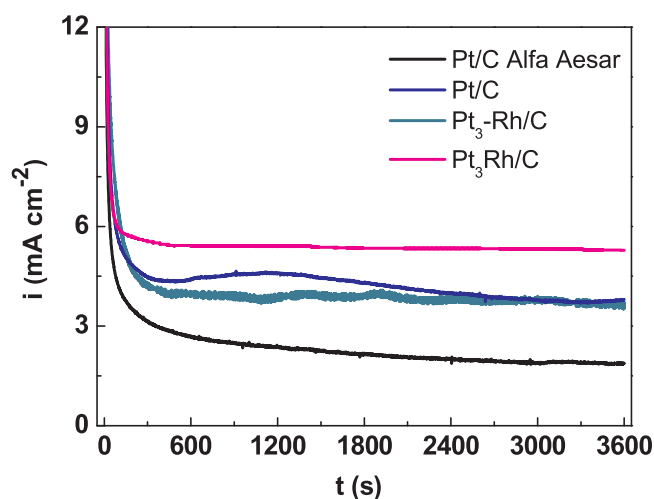

Fig. 8. Chronoamperograms after application of 500 mV for Pt/C Alfa Aesar, Pt/C, Pt$_3$–Rh/C and Pt$_3$Rh/C catalysts in 0.5 mol L^{-1} H$_2$SO$_4$ and 0.5 mol L^{-1} ethanol.

decays quickly after the potential step due to the electrical charging of double layer and to a partial poisoning of the active sites on electrode surface [18]. Intermediate species (CO, CH_x, CH_3CHO and CH_3COOH) formed in the first stages can be responsible for catalysts poisoning [53]. This behaviour was followed by a slow shift towards a quasi-stationary state after the first 500 s.

Here is important to note that our results cannot be compared with the state-of-the-art currents observed for Direct Ethanol Fuel Cells, since we are analysing pseudo-stationary currents in half-cell experiments, while DAFCS use hydrodynamics experiments. Furthermore, we used lower concentrations of ethanol than those adopted for DAFCs, in order to prevent the self-inhibition caused by the excess of surface adsorbates at high concentrations of ethanol [45].

At the end of the experiment, the catalysts had the following electrocatalytic activity order: $Pt_3Rh/C > Pt/C > Pt_3–Rh/C > Pt/C$ Alfa Aesar. Pt/C was more stable in comparison with Pt/C Alfa Aesar probably due to the higher ordering and distribution of Pt atoms on the carbon support surface as previously suggested [58].

The current densities for Pt/C and $Pt_3–Rh/C$, 3.8 and 3.7 mA cm^{-2}, respectively, were approximately 2 times higher than for the commercial catalyst (1.9 mA cm^{-2}). It is known that Rh develops oxide-hydroxide compounds at lower potentials that aid the oxidation of ethanol. However, this effect depends on structural conditions such as interatomic distances. Hence, as the Pt and Rh atoms at $Pt_3–Rh/C$ are not forming an alloy, the beneficial effects of Rh are not effective [22].

The catalytic activity was improved for Pt_3Rh/C, obtaining a current density of 5.3 mA cm^{-2} at the end of the experiment, 3 times higher than the one of the commercial catalyst. Such enhancement is probably due to the substitution of Pt by Rh [26]. Such a significant increase in electrocatalytic activity and stability was also seen in voltammetric curves (Fig. 6), suggesting that the specific structure of Pt_3Rh/C can provide abundant active sites, including defect sites, thereby increasing water and ethanol dissociation [59–61]. These findings are also consistent with XANES results (see Fig. 4 and the corresponding discussion).

Ma et al. [62] synthesized PtSn/C catalysts by using four stabilizers. The chronoamperometric curves recorded at 500 mV in 1.0 mol L^{-1} ethanol for the four catalysts had current densities measured at 900th second between 2.2–3,5 mA cm^{-2}, which were lower than those found in this work for Pt_3Rh/C (5.3 mA cm^{-2}) and $Pt_3–Rh/C$ (3.7 mA cm^{-2}) catalysts, with current densities measured after 3600 s. Li et al. [63] evaluated the stability of Pt_7Sn_3 and Pt nanowires by chronoamperometric tests in 0.5 mol L^{-1} ethanol. The Pt_7Sn_3 alloy nanowires achieve much lower steady-state current densities at a fixed potential of 500 mV *vs.* RHE, about 25 times lower, over the time range of 3600 s, as compared with Pt_3Rh/C catalyst. Pt_3Rh/C and $Pt_3–Rh/C$ catalysts also showed very higher current densities, about one order of magnitude, compared to Pt_1Sn_1/C and Pt_3Sn_1/C (0.15 mA cm^{-2}) catalysts supported on carbon black, reported by Asgardi et al. [64]. The current-time experiments were recorded at 550 mV in 0.5 mol L^{-1} H_2SO_4 + 2.0 mol L^{-1} ethanol.

Furthermore, electrochemical stability tests performed on the materials by chronoamperometry are shown in Fig. S4. The current density for all catalysts decays quickly in the first hours of the experiment. After 70 h, the current density for the Pt/C Alfa Aesar catalyst reaches 0 mA cm^{-2}. Intermediate species formed during ethanol oxidation can be responsible for the total blocking of the catalyst active sites. However, the Pt/C, Pt_3Rh/C and $Pt_3–Rh/C$ catalysts showed fairly high current densities compared to the commercial Pt/C Alfa Aesar catalyst. The PtRh catalysts presented greater poisoning resistance compared to the other catalysts at the end of 100 h. Pt_3Rh/C and $Pt_3–Rh/C$ display current densities of 3.47 mA cm^{-1} and 2.29 mA cm^{-1}, respectively, which were about 2.7 and 1.8 times higher than for the Pt/C catalyst.

Cyclic voltammograms were performed before and after the stability tests in order to evaluate the electroactive area of the materials (Fig. 9). Changes in the voltammetric profile of all catalysts are observed after

100 h of the experiment. Such changes may be related to Pt dissolution, to the accumulation of poisonous species on electrode surface during the experiment, or to the presence of electrolyte organic impurities and/or to Pt atoms reconstruction [65]. The electroactive area for Pt/C Alfa Aesar decreases 50% after 100 h of the experiment indicating low electrochemical stability. This behaviour may be due to Pt dissolution [52,66]. For Pt/C catalyst, (Fig. 9) after 100 h, the peak intensity of hydrogen adsorption/desorption region decreases due to Pt atoms reconstruction or accumulation of poisonous species on electrode surface [46,65,66].

For $Pt_3–Rh/C$, in addition to the possible Pt dissolution, the attenuation of the characteristic peak of catalysts containing rhodium located at 550 mV suggests Rh dissolution [61]. Differently, the loss of electroactive area for Pt_3Rh/C may be related to the blocking of active sites of Pt by Rh atoms, since the characteristic peak of catalysts containing rhodium located at 550 mV, is poorly visible in the initial voltammogram, but it becomes better defined after 100 h. Together with the lower definition of the peak at 270 mV, are indications of hydrogen desorption sites loss in Pt–Rh phases and increases in desorption on pure Rh [67].

Among the catalysts, Pt_3Rh/C showed the highest electrochemical stability. Were observed reductions of 36, 16 and 12% in the initial electroactive area after 100 h of stability test, respectively for the Pt/C, $Pt_3–Rh/C$ and Pt_3Rh/C catalysts. Consequently, the lower stability obtained for $Pt_3–Rh/C$ may be related to the existence of separated Pt and Rh monometallic particles [18]. Notably, Pt_3Rh/C, besides being the most active catalyst is also the most stable one. Thus, it represents a promising alternative for the commercial viability of fuel cell technologies because of their significantly higher electrochemical stability.

3.3. In situ FTIR studies

Considering the results obtained during the voltammetric and stability tests, Fig. 10 shows *in situ* FTIR reflectance spectra for Pt/C, $Pt_3–Rh/C$ and Pt_3Rh/C. The spectra were collected in $HClO_4$ solution to avoid the adsorption of sulphate ions that could hinder the detection of ethanol or other by-products. Down-pointing (negative) bands indicate the production of species in the thin layer formed between the working electrode and the CaF_2 flat window, while up-pointing (positive) bands represent the consumption/depletion of species.

Fig. 10.

The major bands related to the presence of products and intermediates are listed in Table 2. The presence of CO_2, acetaldehyde and acetic acid was observed in all surfaces. The qualitative features are basically the same for all catalysts, being the differences mainly associated with the relative band intensities.

The positive band located at 1650 cm^{-1}, assigned to the water H−O−H bending mode, dominates all the IR spectra [2]. Water is the oxygen donor (Eq. 14), necessary for alcohols oxidation to CO_2; however, it also competes with the organic molecules for adsorption sites [7].

The positive band located at 1045 cm^{-1} indicates that ethanol is consumed from the thin layer as the potential of the electrode increases. The consumption of ethanol was also detected from other band detected at 2908 cm^{-1}, which are ascribed to ethanol asymmetric CH_2 vibrations [68].

Negative bands at 2343 cm^{-1} and 1280 cm^{-1} are respectively attributed to CO_2 formation, with C−C bond breaking and acetic acid formation, maintaining intact the C−C bond [3]. CO_2 formation starts from 600 mV for Pt/C (Fig. 10a) and accelerates with increasing potential. The CO_2 production starts at 250 and 150 mV for $Pt_3–Rh/C$ (Fig. 10b) and Pt_3Rh/C (Fig. 10c) catalysts, respectively. In addition, the band intensity of CO_2 for the alloy containing Rh is higher than for the other catalysts. As previously mentioned [9,13,19,73], the Pt 5*d* band is the relevant one regarding chemisorption and, therefore, changes in its electronic occupancy might weaken the Pt–CO binding
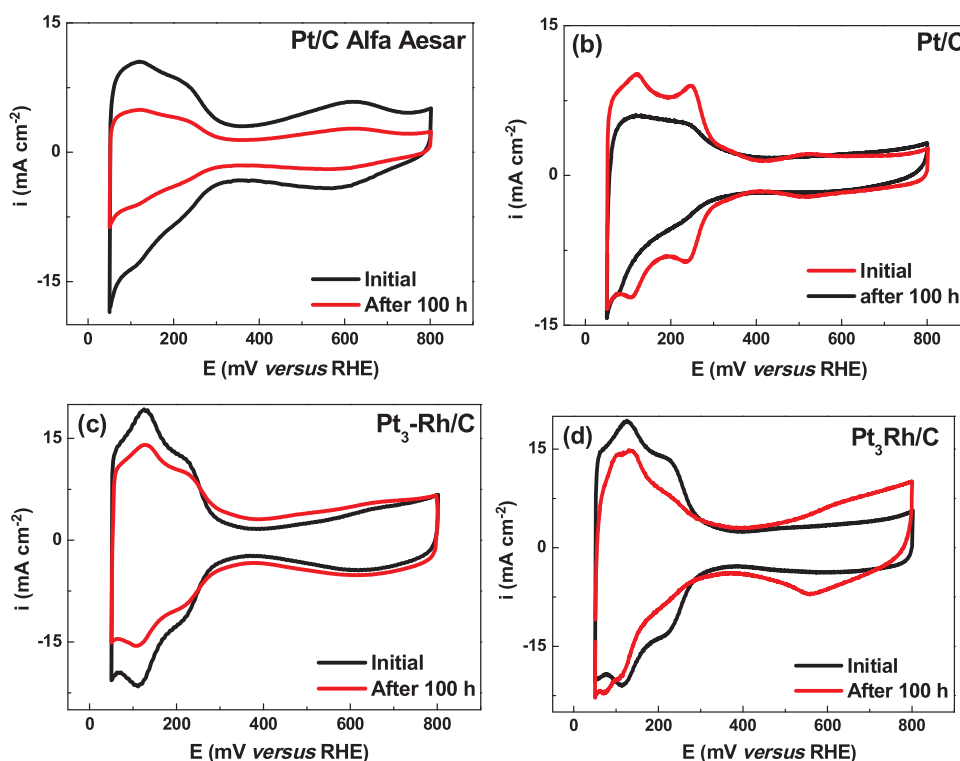
Fig. 9. Cyclic voltammogram curves (second cycle) of Pt/C Alfa Aesar, Pt/C, Pt$_3$–Rh/C and Pt$_3$Rh/C catalysts before and after 100 h of stability test by applying 600 mV. Measurements were carried out in 0.5 mol L^{-1} H$_2$SO$_4$ at room temperature and a scan rate of 10 mV s^{-1}.

energy [78], facilitating CO$_{ads}$ oxidation and increasing CO$_2$ production. Consequently, this enhanced activity agrees with XANES data (Fig. 4) where the largest difference in the whiteline was observed for the Pt$_3$Rh/C catalyst compared with pure Pt/C and Pt$_3$-Rh/C (mixture).

Acetic acid formation becomes evident from the bands located at 2621 cm^{-1}, attributed to the asymmetric stretching of the (−CH$_3$) groups, at 1400 cm^{-1} related to (−OH) deformation groups and at 1280 cm^{-1} associated to (C−O) stretching groups. These bands appear only at potentials higher than 600 mV in all catalysts. The appearance of the band at 1400 cm^{-1} at high potentials values was identified as the adsorbed acetate, indicating that it is an intermediate of ethanol oxidation reaction [2,79].

The bands at 1368 and 1113 cm^{-1} can be associated with symmetric deformation (−CH$_3$) and vibration (C−H), respectively of acetaldehyde [26]. However, the C−H wagging vibration in CH$_3$CHO, at 1113 cm^{-1}, overlaps with the strong band at 1110 cm^{-1} of (Cl−O) stretching vibration in ClO$_4^-$. The latter band is the consequence of ClO$_4^-$ accumulation in the thin layer cell to compensate the charge at the electrode surface under increasingly electrode potential.

For a better comparison of CO$_2$ selectivity for all catalysts, the area of the absorption bands at 2343 cm^{-1}, 1400 cm^{-1} and 1280 cm^{-1} were integrated and further normalized by the electroactive area of each electrode, obtained by the CO oxidation tests (Fig. 11).

The production of CO$_2$ starts only at 600 mV vs RHE for Pt/C catalysts (Fig. 11a). For Pt$_3$–Rh/C (Fig. 11b) and Pt$_3$Rh/C catalyst (Fig. 11c) the first bands appear at 350 and 250 mV, respectively. These results agree with previous ones reported in the literature [2,3], demonstrating that Rh facilitates the C−C bond breaking, favouring the complete ethanol electrooxidation at lower potentials. The band intensity of CO$_2$ for Pt$_3$Rh/C exhibits a higher intensity compared to the bands assigned to acetaldehyde and acetic acid for potentials up to 1000 mV. However, for Pt$_3$-Rh/C as the potential increases to 700 mV, the bands for acetate production become more intense. Thus, the higher selectivity of the PtRh catalyst (alloy) for the formation of CO$_2$ compared to the Pt-Rh (bimetallic mixture) catalyst may be related to the

changes in architectural configurations, which alter the electronic structures of the surface metals. For Pt/C catalysts, the CO$_2$ band intensity is lower than the other bands, demonstrating that C$_2$ path, which maintains the C−C bond intact, is dominant for this surface [80].

When compared with other catalysts commonly studied for the oxidation of ethanol such as PtRu/C and PtSn/C, although decrease the oxidation onset potential of ethanol, they do not favour its complete oxidation to CO$_2$ [81–83]. Wang et al. [81] studied the electrocatalytic activity of PtRu/C and Pt$_3$Sn/C for ethanol oxidation in acid media, using DEMS. Their results showed that the addition of Ru or Sn in Pt catalysts lowers the onset potential of ethanol reaction, but does not improve the selectivity towards CO$_2$ production, which was about 1% for all catalysts. For example, the onset potential for CO$_2$ formation on Pt$_3$Sn/C and PtRu/C catalysts in the positive-going scan is shifted negatively by 100 mV relative to the Pt/C catalyst, from 500 to 400 mV, which are 50 and 150 mV higher than Pt$_3$–Rh/C and Pt$_3$Rh/C catalysts, respectively. Moreover, at potentials of 550 mV, the CO$_2$ formation on PtRu/C and Pt$_3$Sn/C is much lower than for Pt/C; however, at the same potential, CO$_2$ is the only product observed on Pt$_3$-Rh/C and Pt$_3$Rh/C catalysts (Fig. 11).

The in situ FTIR data in Fig. 11 are more expressive than that presented by Delpeuch et al. [2] for PtRhSnO$_2$/C catalyst, which is considered as an efficient catalyst for the C−C bond breaking and investigated by several authors [26,75]. In that study, the CO$_2$ intensity for PtRhSnO$_2$/C catalyst was higher than the other products only at high potentials, after 650 mV.

The acetic acid production at 1280 cm^{-1} occurred only at potentials higher than 600 mV for Pt/C and at 750 mV for the bimetallic catalysts. This band increased continuously for all the studied catalysts indicating that acetic acid formation occurred through acetaldehyde oxidation and/or intermediates such as acetate [56].

The acetate production band at 1368 cm^{-1} was observed at 650 mV for Pt/C and Pt$_3$-Rh$_1$/C and at 850 mV for Pt$_3$Rh/C, Fig. 11. These data demonstrate the greater preference for the C1 pathway for the alloy-type catalyst. For Pt$_3$-Rh$_1$/C, the intensity of this band increased
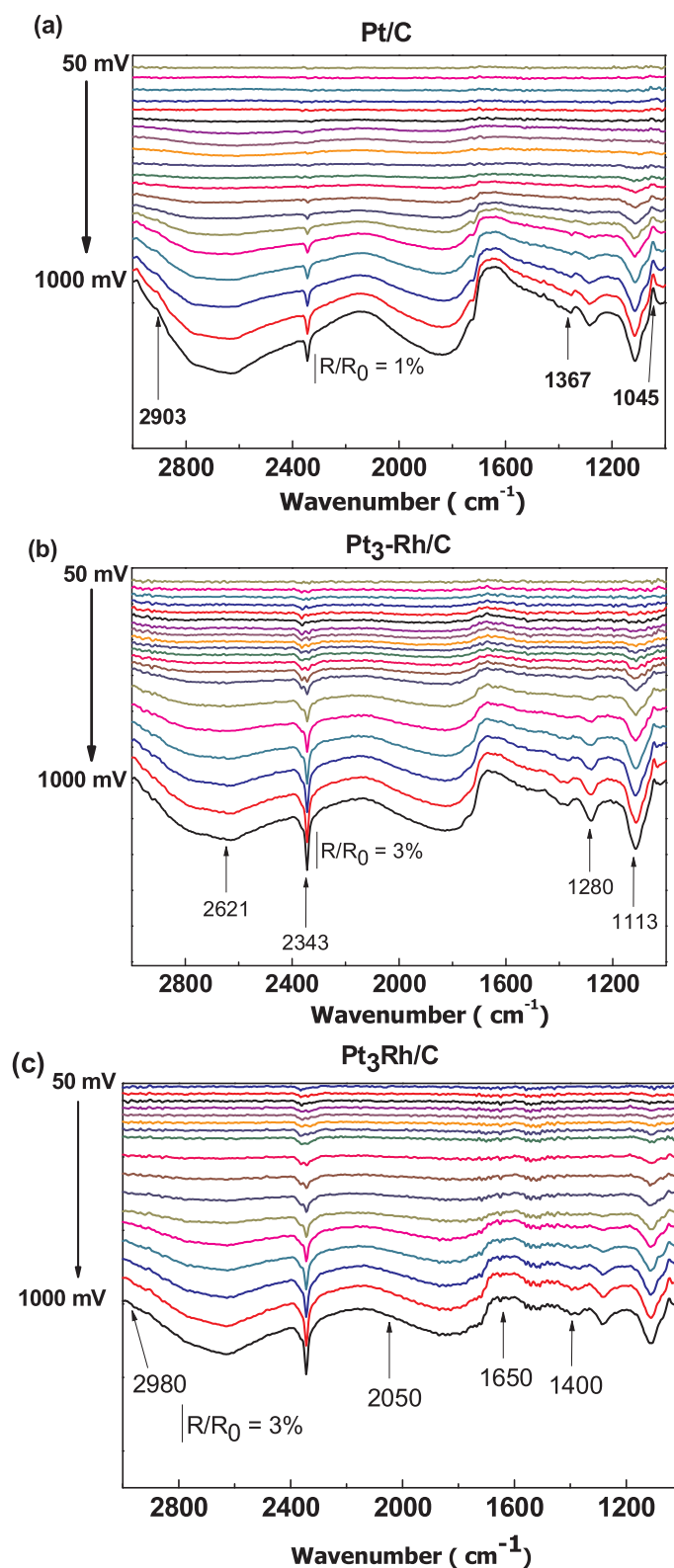
Fig. 10. *In situ* FTIR spectra obtained in 0.1 mol L^{-1} HClO$_4$ + 0.5 mol L^{-1} ethanol for Pt/C, Pt$_3$–Rh/C and Pt$_3$Rh/C catalysts. Reference spectra were taken at 50 mV, collected during a linear sweep voltammogram (ν = 1 mV s^{-1}) in which the potential was paused at each 50 mV for collecting the spectra. Spectral resolution of 8 cm^{-1}.

continuously until reaching 850 mV. However, in higher potentials, there was a sudden decrease in the intensity of this band, followed by a more intense growth in the band at 1280 cm^{-1}, reinforcing the assumption that acetate is an intermediate for the acetic acid formation [26].

The oxidation products yields were calculated using the respectively integrated band intensities (A$_i$), and the amount of species Q (mol cm^{-2}) within the thin layer according to the following relation [76]:

$$Q = A_i/\varepsilon_{eff} \qquad (19)$$

Table 2

Assignment of the bands observed in the spectra obtained by *in situ* FTIR during ethanol oxidation on the Pt/C, Pt₃–Rh/C and Pt₃Rh₁/C surfaces.

Wavenumber (cm⁻¹)	Species	Assignment	References
2980, 2903	CH_3, CH_2	C–H, stretching	[69]
2621	COOH	O–H, stretching	[70]
2343	CO_2	O = C = O, asymmetric stretching	[2,70]
2050	CO_L	–C–O, stretching	[71]
1650	H_2O	H–O–H, bending	[2,72]
1400	Acetate	–O–C–O, stretching	[73]
1368	Acetaldehyde	CH_3, symmetric deformation and wagging C-H	[73]
1280	Acetic acid	–C = O, stretching	[70]
1110	Perchlorate	Cl-O, stretching vibration	[73,74]
1045	Ethanol	C–O, axial deformation	[75,76,77]

The values of the specific absorption coefficient, ε_{eff}, were taken from the reports of Gao *et al.* [80] and Leung et al. [84], which were $3.5 \times 10^4 \, M^{-1} \, cm^{-2}$ for CO_2 and $5.8 \times 10^3 \, M^{-1} \, cm^{-2}$ for acetic acid. CO_2 and acetic acid amounts obtained for Pt/C, Pt₃–Rh/C and Pt₃Rh/C catalysts are shown in Fig. 12. The CO_2 production for Pt/C catalyst is very low, even at high potentials, as is shown in Fig. 12a. Up to 700 mV, acetic acid production was dominant.

For Pt₃Rh/C catalyst (Fig. 12c) the behaviour is different, at low potentials, up to 150 mV, CO_2 appears as the main product formed during ethanol oxidation, evidenced from the insert of Fig. 12c, demonstrating Rh ability to break the C–C bond. With an increasing potential for values above 850 mV, the production of intermediates such as acetic acid is predominant. It is important to emphasize the possibility of a minor interference from atmospheric CO_2 during the experiments and, therefore, the data must be interpreted with some precaution. It is noteworthy that the second peak (peak c″) found for Pt₃Rh/C catalyst during derivative voltammetry in Fig. 7b at 700 mV coincides with CO_2 production observed in Fig. 12c. The complete ethanol oxidation to CO_2 releases 12 electrons, whereas partial oxidation generates only 4 electrons *via* acetic acid production or *via* acetaldehyde, providing 2 electrons [85]. This may explain the higher intensity of peak c″ in comparison to peak c, since CO_2 production was high in this potential range than the other bands.

Therefore, for Pt₃Rh/C catalyst, the synergy between Pt and Rh alloy structure effects was effective in C–C bond breaking of ethanol, causing CO_2 formation at low potentials and high current density values.

4. Conclusions

We herein report the synthesis of catalysts containing Pt and Rh (bimetallic mixture and alloy) to study the effect of Pt-Rh bimetallic structure on the catalytic activity towards ethanol oxidation in acid media as well as the formation of reaction intermediates. The nanoparticles synthesized were active for ethanol electrochemical oxidation. The catalytic activity towards ethanol oxidation depends on the catalyst structure.

For the alloy catalyst (Pt₃Rh/C), the addition of Rh generates high current densities (in a quasi-steady-state condition) for ethanol oxidation, about 5.2 times higher than Pt monometallic catalyst. Thus, the higher catalytic activity obtained for the Pt₃Rh/C catalyst can be attributed to the electronic and geometric effects, confirmed by XANES data, induced by the Pt–Rh alloy. Pt/C and Pt₃–Rh/C catalysts also present current densities higher than the Pt/C Alfa Aesar catalyst. The bimetallic catalysts demonstrate high electrochemical stability after 1000 voltammetric cycles when compared to the commercial one. Pt₃Rh/C displayed the highest stability among the developed catalysts. Chronoamperometric tests also reveal higher stability and poisoning
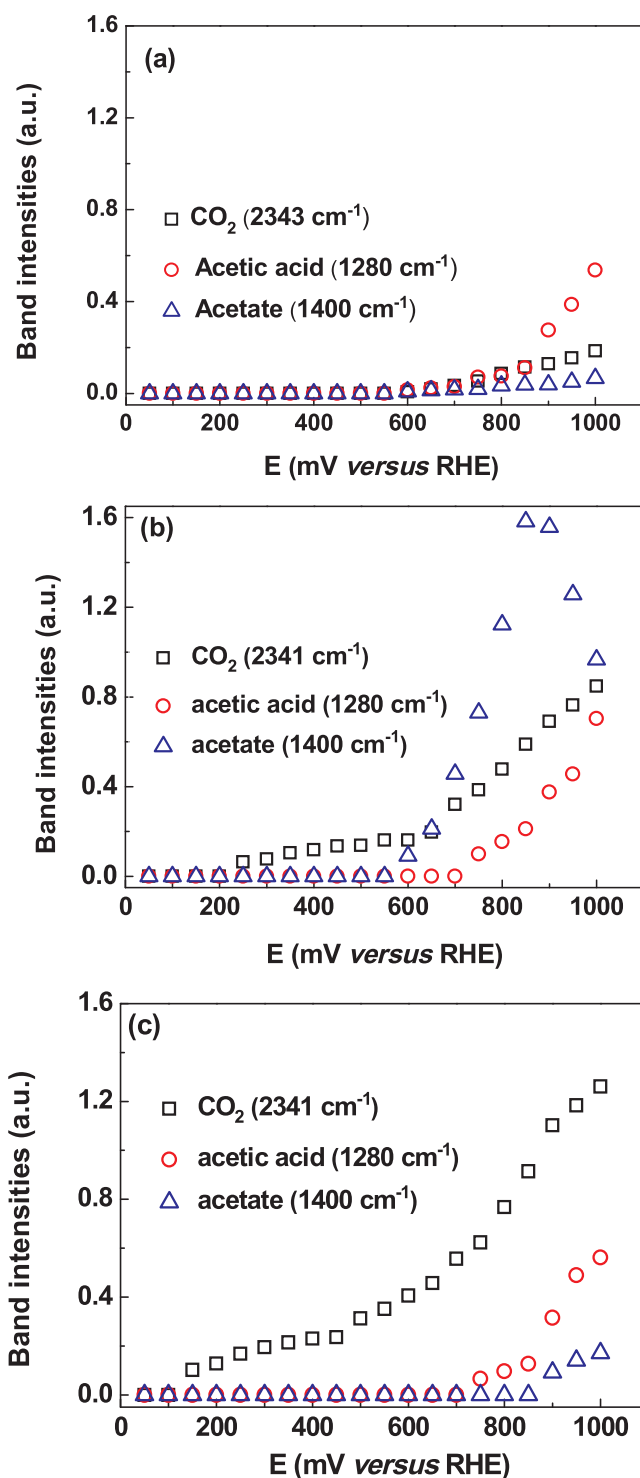

Fig. 11. Infrared bands intensity as a function of electrode potential for Pt/C (a), Pt₃–Rh/C (b) and Pt₃Rh/C (c) catalysts. The bands at 2343, 1400 and 1280 cm⁻¹ represent the production of CO_2, acetate and acetic acid, respectively. The data were calculated from the FTIR spectra.

resistance for bimetallic catalysts, especially Pt₃Rh/C, which present the highest current densities at the end of the experiment, 3 times higher than Pt/C Alfa Aesar.

According to *in situ* FTIR data, the onset potential of the ethanol oxidation reaction for the rhodium-containing catalysts are 350 and 450 mV lower on Pt₃-Rh/C (mixture) and Pt₃Rh/C (alloy) respectively, than for Pt/C. CO_2 production also occurs at low potentials, starting at
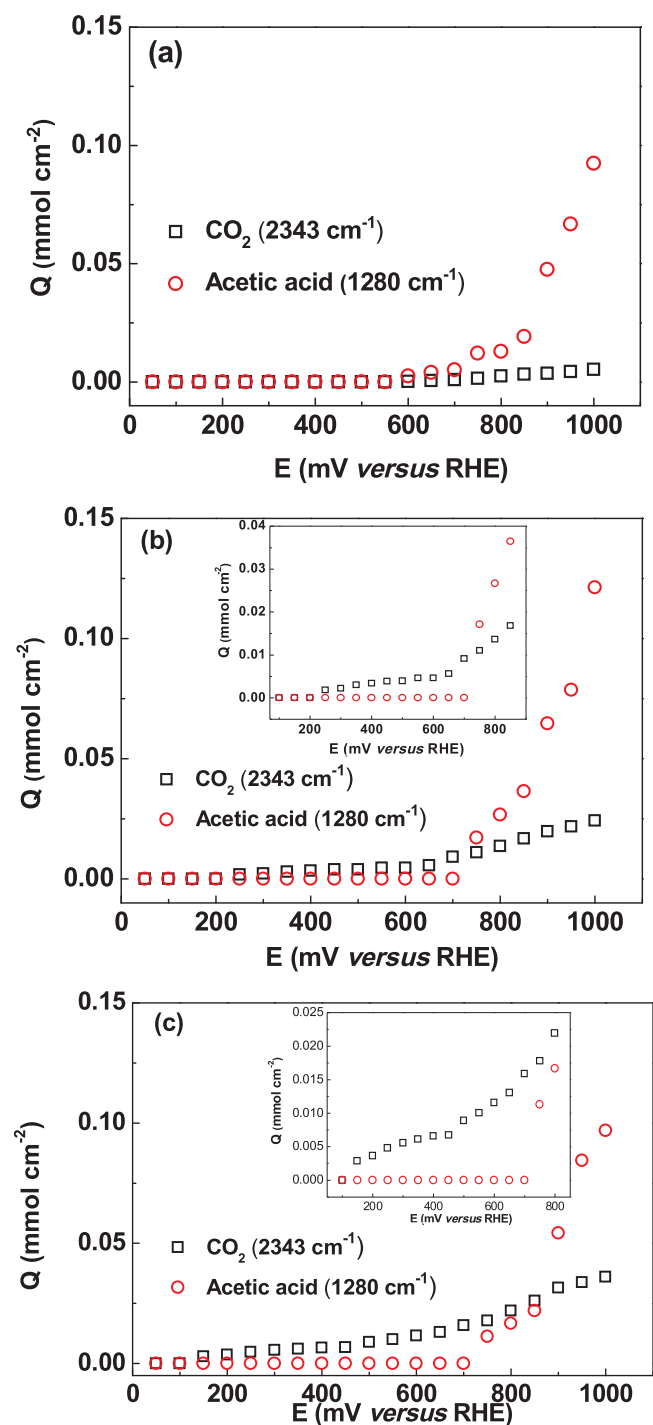
Fig. 12. Quantities (Q) of CO_2 (2343 cm^{-1}) and acetic acid (1280 cm^{-1}) produced during ethanol oxidation as a function of the potential applied to the catalysts (a) Pt/C, (b) Pt$_3$–Rh/C, (c) Pt$_3$Rh/C. Insert: Area approximation between.50–800 mV.

250 mV for Pt$_3$Rh/C catalyst. Estimations of oxidation products show that acetic acid is the major product formed over Pt/C. For Pt$_3$Rh/C, up to 850 mV, C−C bond breaking and CO_2 production is the dominant reaction, but with increasing potential, acetate production and, in larger quantities, acetic acid became the main reactions. The superior catalytic performance and the higher selectivity for CO_2 formation at low potentials for Pt$_3$Rh/C catalyst can be attributed to the synergy between the metals and the presence of alloy structure.

Appendix B. Supplementary data

Supplementary material related to this article can be found, in the online version, at doi:https://doi.org/10.1016/j.apcatb.2019.04.078.

References

[1] L.A. Soares, C. Morais, T.W. Napporn, K.B. Kokoh, P. Olivi, Beneficial effects of rhodium and tin oxide on carbon supported platinum catalysts for ethanol electrooxidation, J. Power Sources 315 (2016) 47–55.

[2] A.B. Delpeuch, F. Maillard, M. Chatenet, P. Soudant, C. Cremers, Ethanol oxidation reaction (EOR) investigation on Pt/C, Rh/C, and Pt-based bi- and tri-metallic electrocatalysts: a DEMS and in situ FTIR study, App. Catal. B: Environ. 181 (2016) 672–680.

[3] E.A. De Souza, M.J. Giz, G.A. Camara, E. Antolini, R.R. Passos, Ethanol electrooxidation on partially alloyed Pt–Sn–Rh/C catalysts, Electrochim. Acta 147 (2014) 483–489.

[4] F. Vigier, C. Coutanceau, F. Hahn, E.M. Belgsir, C. Lamy, On the mechanism of ethanol electro-oxidation on Pt and PtSn catalysts: electrochemical and *in situ* Ir reflectance spectroscopy studies, Electroanal. Chem. 563 (2004) 81–89.

[5] T. Sheng, W.F. Lin, C. Hardacre, P. Hu, Role of water and adsorbed hydroxyls on ethanol electrochemistry on Pd: new mechanism, active centers, and energetics for direct ethanol fuel cell running in alkaline medium, J. Phys. Chem. C 118 (2014) 5762–5772.

[6] V.P. Dos Santos, G.T. Filho, Correlação entre a estrutura atômica superficial e o processo de adsorção-dessorção reversível de hidrogênio em eletrodos monocristalinos de Pt (111), Pt (100) e Pt (110), Quim. Nova 24 (2001) 856–863.

[7] T. Iwasita, Fuel cells: spectroscopic studies in the electrocatalysis of alcohol oxidation, J. Braz. Chem. Soc. 13 (2002) 401–409.

[8] K. Fatih, V. Neburchilov, V. Alzate, R. Neagu, H. Wang, Synthesis and characterization of quaternary PtRuIrSn/C electrocatalysts for direct ethanol fuel cells, J. Power Sources 195 (2010) 7168–7175.

[9] D. Chen, Y. Li, S. Liao, D. Su, H. Song, Y. Li, L. Yang, C. Li, Ultra-high-performance core-shell structured Ru@Pt/C catalyst prepared by a facile pulse electrochemical deposition method, Sci. Rep. 5 (2015) 11604–11612.

[10] L.S.R. Silva, F. López-Suárez, M. Perez-Cadenas, S.F. Santos, L.P. Da Costa, K.I.B. Eguiluz, G.R. Salazar-Banda, Synthesis and characterization of highly active Pb$_x$@Pt$_y$/C core–shell nanoparticles toward glycerol electrooxidation, App. Catal. B: Environ. 198 (2016) 38–48.

[11] N. Muthuswamy, J.L.G. De La Fuente, D.T. Tran, J. Walmsley, M. Tsypkin, S. Raaen, S. Sunde, M. Rønning, D. Chen, Ru@Pt core–shell nanoparticles for methanol fuel cell catalyst: control and effects of shell composition, Int. J. Hydrogen Energy 38 (2013) 16631–16641.

[12] N. Zhang, S. Guo, X. Zhu, J. Guo, X. Huang, Hierarchical Pt/Pt$_x$Pb core/shell nanowires as efficient catalysts for electrooxidation of liquid fuels, Chem. Mater. 28 (2016) 4447–4452.

[13] X. Zhang, H. Wang, J. Key, V. Linkov, S. Ji, X. Wang, Z. Lei, R. Wang, Strain effect of core–shell Co@Pt/C nanoparticle catalyst with enhanced electrocatalytic activity for methanol oxidation, J. Electrochem. Soc. 159 (2012) 207–276.

[14] W. Zhu, J. Ke, S.-B. Wang, J. Ren, H.-H. Wang, Z.-Y. Zhou, R. Si, Y.-W. Zhang, C.-H. Yan, Shaping single-crystalline trimetallic Pt–Pd–Rh nanocrystals toward high-efficiency C–C splitting of ethanol in conversion to CO_2, ACS Catal. 5 (2015) 1995–2008.

[15] K. Bergamaski, E.R. Gonzalez, F.C. Nart, Ethanol oxidation on carbon supported Platinum-Rhodium bimetallic catalysts, Electrochim. Acta 53 (2008) 4396–4406.

[16] L.L.A. Souza, G.R.O. Almeida, L.S.R. Silva, F.O.F. Bergamaski, A.S. Lima, K.I.B. Eguiluz, G.R. Salazar-Banda, Outstanding electro-catalytic activity of Pt$_x$–(RuO$_y$–CeO$_2$)$_{1-x}$/C composites towards ethanol oxidation in acid media, J. App. Eletrochem. 43 (2013) 953–965.

[17] P.A. Christensen, S.W.M. Jones, A. Hamnett, In situ FTIR studies of ethanol oxidation at polycrystalline Pt in alkaline solution, J. Phys. Chem. C 116 (2012) 26109–26109.

[18] H.F. Wang, Z.P. Liu, Comprehensive mechanism and structure-sensitivity of ethanol oxidation on platinum: new transition-state searching method for resolving the complex reaction network, J. Am. Chem. Soc. 130 (2008) 10996–11004.

[19] L. Colmenares, H. Wang, Z. Jusys, L. Jiang, S. Yan, G.Q. Sun, R.J. Behm, Ethanol oxidation on novel, carbon supported Pt alloy catalysts-model studies under defined diffusion conditions, Electrochim. Acta 52 (2006) 221–233.

[20] H. Wang, Z. Jusys, R.J. Behm, Ethanol electrooxidation on a carbon-supported Pt catalyst: reaction kinetics and product yields, J. Phys. Chem. B 108 (2004) 19413–19424.

[21] V. Rao, C. Cremers, U. Stimming, Investigation of the ethanol electro-oxidation in alkaline membrane electrode assembly by differential electrochemical mass spectrometry, Fuel Cells 7 (2007) 417–423.

[22] J.P.I. Souza, S.L. Queiroz, K. Bergamaski, E.R. Gonzalez, F.C. Nart, Electro-oxidation of ethanol on Pt, Rh, and PtRh electrodes. A study using DEMS and *in situ* FTIR techniques, J. Phys. Chem. 106 (2002) 9825–9830.

[23] S. Alayoglu, B. Eichhorn, Rh-Pt bimetallic catalysts: synthesis, characterization, and catalysis of core-shell, alloy, and monometallic nanoparticles, J. Am. Chem. Soc. 130 (2008) 17479–17486.

[24] M. Li, A. Kowal, K. Sasaki, N. Marinkovic, D. Su, E. Korach, P. Liu, R.R. Adzic, Ethanol oxidation on the ternary Pt–Rh–SnO$_2$/C electrocatalysts with varied Pt:Rh:Sn ratios, Electrochim. Acta 55 (2010) 4331–4338.

[25] S.S. Gupta, D. Jayati, A comparative study on ethanol oxidation behavior at Pt and PtRh electrodeposits, J. Electroanal. Chem. 594 (2006) 65–72.

[26] L.C. Silva-Junior, G. Maia, R.R. Passos, E.A. De Souza, G.A. Camara, J.M. Giz, Analysis of the selectivity of PtRh/C and PtRhSn/C to the formation of CO$_2$ during ethanol electrooxidation, Electrochim. Acta 112 (2013) 612–619.

[27] E.S. Valério Neto, M.A. Gomes, G.R. Salazar-Banda, K.I.B. Eguiluz, Pt and Pt–Rh nanowires supported on carbon and SnO$_2$:Sb nanoparticles for ethanol electrochemical oxidation in acidic media, Int. J. Hydrogen Energy 43 (2018) 178–188.

[28] B. Ravel, M. Newville, ATHENA, ARTEMIS, HEPHAESTUS: data analysis for X-ray absorption spectroscopy using IFEFFIT, J. Synchrotron Radiat. 12 (2005) 537–541.

[29] M. Watanabe, H. Sei, P. Stonehart, The influence of platinum crystallite size on the electroreduction of oxygen, J. Electroanal. Chem. 261 (1989) 375–387.

[30] D. González-Quijano, W.J. Pech-Rodríguez, J.A. González-Quijano, J.I. Escalante-García, G. Vargas-Gutiérrez, J. Alonso-Lemus, F.J. Rodríguez-Varela, Electrocatalysts for ethanol and ethylene glycol oxidation reactions. Part II: effects of the polyol synthesis conditions on the characteristics and catalytic activity of Pt–Ru/C anodes, I, J. Hydrogen Energy 40 (2015) 17291–17299.

[31] K.I.B. Eguiluz, G.R. Salazar-Banda, D. Miwa, S.A.S. Machado, L.A. Avaca, Effect of the catalyst composition in the Pt$_x$(Ru–Ir)$_{1−x}$/C system on the electro-oxidation of methanol in acid media, J. Power Sources 179 (2008) 42–49.

[32] M. Li, W.-P. Zhou, N.S. Marinkovic, K. Sasaki, R.R. Adzic, The role of rhodium and tin oxide in the Platinum-based electrocatalysts for ethanol oxidation to CO$_2$, Electrochim. Acta 104 (2013) 454–461.

[33] M. Li, N.S. Marinkovic, K. Sasaki, *In situ* characterization of ternary Pt–Rh–SnO$_2$/C catalysts for ethanol electrooxidation, Electrocatalysis 3 (2012) 376–385.

[34] M. Hansen, K. Anderko, New York, Constitution of Binary Alloys, second ed., (1958).

[35] D.W. Inwood, X-Ray and Electrochemical Studies of Bimetallic Pt-Based Oxygen Reduction Electrocatalysts, University of Southampton, 2017 Doctoral Thesis.

[36] H. Angerstein-Kozlowska, B.E. Conway, W.B.A. Sharp, The real condition of electrochemically oxidized platinum surfaces: part I. Resolution of component processes, J. Electroanal. Chem. 43 (1973) 9–36.

[37] X. Xu, W. Wang, W. Zhou, Z. Shao, Recent advances in novel nanostructuring methods of perovskite electrocatalysts for energy-related applications, Small 2 (2018) 1800071–1800106.

[38] B. Xiong, Y. Zhou, Y. Zhao, J. Wang, X. Chen, R. O'Hayre, Z. Shao, The use of nitrogen-doped graphene supporting Pt nanoparticles as a catalyst for methanol electrocatalytic oxidation, Carbon (2013) 181–192.

[39] Y. Zhou, K. Neyerlin, T.S. Olson, S. Pylypenko, J. Bult, H.N. Dinh, T. Gennett, Z. Shao, R. O'Hayre, Enhancement of Pt and Pt-alloy fuel cell catalyst activity and durability via nitrogen-modified carbon supports, Energy Environ. Sci. 3 (2010) 1437–1446.

[40] B. Corain, G. Schmid, N. Toshima, Metal Nanoclusters in Catalysis and Materials Science: The Issue of Size Control, first ed., (2004) Amsterdam, Netherlands.

[41] N.V. Long, M. Ohtaki, T.D. Hien, J. Randy, M. Nogami, A comparative study of Pt and Pt–Pd core–shell nanocatalysts, Electrochim. Acta 58 (2011) 1–38.

[42] J.K. Norskov, T. Bligaard, J. Rossmeisl, C.H. Christensen, Towards the computational design of solid catalysts, Nat. Chem. 1 (2009) 37–46.

[43] F.H.B. Lima, D. Profeti, W.H. Lizcano-Valbuena, E.A. Ticianelli, E.R. Gonzalez, Carbon-dispersed Pt–Rh nanoparticles for ethanol electro-oxidation. Effect of the crystallite size and of temperature, J. Electroanal. Chem. 617 (2008) 121–129.

[44] F. Colmati, G. Tremiliosi-Filho, E.R. Gonzalez, A. Berná, E. Herrero, J.M. Feliu, The role of the steps in the cleavage of the C−C bond during ethanol oxidation on platinum electrodes, Phys. Chem. Chem. Phys. 11 (2009) 9114–9123.

[45] G.A. Camara, T. Iwasita, Parallel pathways of ethanol oxidation: the effect of ethanol concentration, J. Electroanal. Chem. 578 (2005) 315–321.

[46] A. Murthy, A. Manthiram, Application of derivative voltammetry in the analysis of methanol oxidation reaction, J. Phys. Chem. C 116 (2012) 3827–3832.

[47] H. Li, G. Sun, L. Cao, L. Jiang, Q. Xin, Comparison of different promotion effect of PtRu/C and PtSn/C electrocatalysts for ethanol electro-oxidation, Electrochim. Acta 52 (2007) 6622–6629.

[48] M. Zhu, G. Sun, Q. Xin, Effect of alloying degree in PtSn catalyst on the catalytic behavior for ethanol electro-oxidation, Electrochim. Acta 54 (2009) 1511–1518.

[49] P. Mukherjee, P.S. Roy, S.K. Bhattacharya, Improved carbonate formation from ethanol oxidation on nickel supported Pt–Rh electrode in alkaline medium at room temperature, Int. J. Hydrogen Energy 40 (2015) 13357–13367.

[50] J. Tayal, B. Rawat, S. Basu, Bi-metallic and tri-metallic Pt–Sn/C, Pt–Ir/C, Pt–Ir–Sn/C catalysts for electro-oxidation of ethanol in direct ethanol fuel cell, Int. Hydrogen Energy 36 (2011) 14884–14897.

[51] J. Perez, V.A. Paganin, E. Antolini, Particle size effect for ethanol electro-oxidation on Pt/C catalysts in half-cell and in a single direct ethanol fuel cell, J. Electroanal

[52] E. Antolini, Structural parameters of supported fuel cell catalysts: the effect of particle size, inter-particle distance and metal loading on catalytic activity and fuel cell performance, Appl. Catal. B: Environ. 181 (2016) 298–313.

[53] C. Xu, Y. Liu, J. Wang, H. Geng, H. Qiu, Fabrication of nanoporous Cu–Pt(Pd) core@shell structure by galvanic replacement and its application in electrocatalysis, Appl. Mater. Interfaces 3 (2011) 4626–4632.

[54] G. Li, P.G. Pickup, Decoration of carbon-supported Pt catalysts with Sn to promote electro-oxidation of ethanol, J. Power Sources 173 (2007) 121–129.

[55] F. Colmati, E. Antolini, E.R. Gonalez, Ethanol oxidation on carbon supported Pt–Sn electrocatalysts prepared by reduction with formic acid, J. Electrochem. Soc. 154 (2007) 39–47.

[56] P.G. Corradini, E. Antolini, J. Perez, Activity, short-term stability (poisoning tolerance) and durability of carbon supported Pt–Pr catalysts for ethanol oxidation, J. Power Sources 251 (2014) 402–410.

[57] O. Guillén-Villafuerte, G. García, M.C. Arévalo, J.L. Rodríguez, E. Pastor, New insights on the electrochemical oxidation of ethanol on carbon-supported Pt electrode by a novel electrochemical mass spectrometry configuration, Electrochem. commun. 63 (2016) 48–51.

[58] L. Da Silva, E. Cuña, A.R.O. Vega, M. Radtke, C. Machado, G. Tancredi, C.N.F. Malfatti, Influence of the support on PtSn electrocatalysts behavior: ethanol electro-oxidation performance and in-situ ATR-FTIRS studies, App. Catal. B: Environ. 193 (2016) 170–179.

[59] Y.-Y. Yang, J. Ren, Q.-X. Li, Z.-Y. Zhou, S.-G. Sun, W.-B. Cai, Electrocatalysis of ethanol on a Pd electrode in alkaline media: an in situ attenuated total reflection surface-enhanced infrared absorption spectroscopy study, ACS Catal. 4 (2014) 798–803.

[60] H.A. Asiri, A.B. Anderson, Mechanisms for ethanol electrooxidation on Pt(111) and adsorption bond strengths defining an ideal catalyst, J. Electrochem. Soc. 162 (2015) F115–F122.

[61] N. Tian, Z. Zhou, S. Sun, Y. Ding, Z. Wang, Synthesis of tetrahexahedral platinum nanocrystals with high-index facets and high electro-oxidation activity, Science 316 (2007) 731–735.

[62] Y. Ma, H. Wang, S. Ji, V. Linkov, R. Wang, PtSn/C catalysts for ethanol oxidation: the effect of stabilizers on the morphology and particle distribution, J. Power Sources 247 (2014) 142–150.

[63] L. Li, H. Liu, C. Qin, Z. Liang, A. Scida, S. Yue, X. Tong, R.R. Adzic, S.S. Wong, Ultrathin Pt$_x$Sn$_{1−x}$ nanowires for methanol and ethanol oxidation reactions: tuning performance by varying chemical composition, ACS Appl. Nano Mater. 1 (2018) 1104–1115.

[64] J. Asgardia, J.C. Calderón, F. Alcaide, A. Querejeta, L. Calvillo, M.J. Lázaro, G. García, E. Pastor, Carbon monoxide and ethanol oxidation on PtSn supported catalysts:effect of the nature of the carbon support and Pt:Sn composition, App. Catal. B: Environ. 168–169 (2015) 33–41.

[65] B. Zhang, D. Wang, Y. Hou, S. Yang, X.H. Yang, J.H. Zhong, J. Liu, H.F. Wang, P. Hu, H.J. Zhao, H.G. Yang, Facet-dependent catalytic activity of platinum nanocrystals for triiodide reduction in dye-sensitized solar cells, Sci. Rep. 3 (2013) 1836–1843.

[66] R. Devivaraprasad, T. Kar, A. Chakraborty, R.K. Singh, M. Neergat, M. Neergat, T. Kinumoto, Y. Iriyama, Z. Ogumi, Y. Iwasawa, H. Zheng, Reconstruction and dissolution of shape-controlled pt nanoparticles in acidic electrolytes, Phys. Chem. Chem. Phys. 18 (2016) 11220–11232.

[67] F.J. Vidal-Iglesias, R.M. Aran-Ais, J. Solla-Gullon, E. Herrero, J.M. Feliu, Electrochemical characterization of shape-controlled Pt nanoparticles in different supporting electrolytes, ACS Catal. 2 (2012) 901–910.

[68] F.H.B. Lima, E.R. Gonzalez, Ethanol electro-oxidation on carbon-supported Pt–Ru, Pt–Rh and Pt–Ru–Rh nanoparticles, Electrochim. Acta 53 (2008) 2963–2971.

[69] G. Sócrates, Infrared and Raman Characteristic Group Frequencies: Tables and Charts, third ed., Willey, Chichester, United Kingdom, 2001.

[70] G. Sócrates, Infrared and Raman Characteristic Group Frequencies: Tables and Charts, fourth ed., Willey, Chichester, United Kingdom, 2004.

[71] A. Bewick, K. Kunimatsu, S. Pons, Infrared-spectroscopy of the electrode–electrolyte interphase, Electrochim. Acta 25 (1980) 465–468.

[72] J.F. Gomes, G. Tremiliosi-Filho, Spectroscopic studies of the glycerol electro-oxidation on polycrystalline Au and Pt surfaces in acidic and alkaline media, Electrocatalysis 2 (2011) 96–102.

[73] M. Li, W.-P. Zhou, N.S. Marinkovic, K. Sasaki, R.R. Adzic, The Role of rhodium and tin oxide in the platinum-based electrocatalysts for ethanol oxidation to CO$_2$, Electrochim. Acta 104 (2013) 454–461.

[74] J.G. Wu, Modern Fourier Transform Infrared Spectroscopy Techniques and their Applications, first ed., Elsevier Science, London, United Kingdom, 1994.

[75] M.E. Paulino, L.M. Nunes, E.R. Gonzalez, G. Tremiliosi-Filho, *In situ* FTIR spectroscopic study of ethanol oxidation on Pt (111)/Rh/Sn surface: the anion effect, Electrochem. commun. 52 (2015) 85–88.

[76] R.M. Silverstein, F.X. Webster, D.J. Kiemle, Spectrometric Identification of Organics Compounds, seventh ed., Willey, Hoboken, New Jersey, 2005.

[77] J.M. Perez, B. Beden, F. Hahn, A. Aldaz, C. Lamy, "In Situ" Infrared Reflectance Spectroscopic study of the early stages of ethanol adsorption at a platinum electrode in acid medium, J. Electroanal. Chem. 262 (1989) 251–261.

[78] L. Li, M. Chen, G. Huang, N. Yang, L. Zhang, H. Wang, Y. Liu, W. Wang, J. Gao, A green method to prepare Pd–Ag nanoparticles supported on reduced graphene oxide and their electrochemical catalysis of methanol and ethanol oxidation, J. Power Sources 263 (2014) 13–21.

[79] E. Pastor, T. Iwasita, D/H exchange of ethanol at platinum electrodes, Electrochim. Acta 39 (1994) 547–551.

[80] P. Gao, S.C. Chang, Z.H. Zhou, M.J. Weaver, Electrooxidation pathways of simple

alcohols at platinum in pure non-aqueous and concentrated aqueous environments as studied by real-time FTIR spectroscopy, J. Electroanal. Chem. 272 (1989) 161–178.

[81] H. Wang, Z. Jusys, R.J. Behm, Ethanol electro-oxidation on carbon-supported Pt, PtRu and Pt$_3$Sn catalysts: a quantitative DEMS study, J. Power Sources 154 (2006) 351–359.

[82] S. Rousseau, C. Coutanceau, C. Lamy, J.-M. Léger, Direct ethanol fuel cell (DEFC): electrical performances and reaction products distribution under operating conditions with different platinum-based anodes, J. Power Sources 158 (2006) 18–24.

[83] R. Alcala, J.W. Shabaker, G.W. Huber, M.A. Sanchez-Castillo, J.A. Dumesic, Experimental and DFT studies of the conversion of ethanol and acetic acid on PtSn-based catalysts, J. Phys. Chem. B 109 (2005) 2074–2085.

[84] L.W.H. Leung, S.C. Chang, M.J. Weaver, Real-time FTIR spectroscopy as an electrochemical mechanistic probe-electrooxidation of ethanol and related species on well-defined Pt (111) surfaces, J. Electroanal. Chem. 266 (1989) 317–336.

[85] S.C.S. Lai, S.E.F. Kleijn, F.T.Z. Öztürk, V.C. van Ress Vellinga, J. Koning, P. Rodriguez, M.T.M. Koper, Effects of electrolyte pH and composition on the ethanol electro-oxidation reaction, Catal. Today 154 (2010) 92–104.